THE UNIVERSITY OF HONG KONG

MASTER THESIS

Intelligent Soft Shape Sensing from Sparse to Dense in Real Time

MAK Chi Hin

A thesis submitted in fulfillment of the requirements

for the degree of Master of Philosophy

in the

Department of Mechanical Engineering

Faculty of Engineering

August 7, 2023

Abstract of thesis entitled

Intelligent Soft Shape Sensing from Sparse to Dense in Real Time

Submitted by

MAK Chi Hin

for the degree of Master of Philosophy

at The University of Hong Kong

in August, 2023

Soft sensor, as a key component in wearable devices and soft robots, has been prevalent recently in various research fields such as smart prosthetics, surgical manipulators and intelligent robotic system. The inherent mechanical compliance and adaptability of soft sensor allow data collection over a deformed medium without any physical mismatches and motion artifacts commonly occurring in its conventional rigid counterparts. It opens up many new challenges and opportunities to enhance the sensing capability of human perception as well as robotic proprioception. The primary motivation of this thesis initiated from the challenge of designing a high-dimensional soft sensor, which is capable of sensing 3-D morphological changes. The research gap in modeling a soft shape sensor is addressed based on literature reviews on the recent advances of flexible electronics, optical-based sensing, as well as a machine learning method. Upon developing shape sensing prototypes, this thesis also investigates how to scale up the sensing area without compromising sensitivity and update frequency.

In the first study, a data-driven modeling approach was explored to reconstruct the morphological changes of a thin, A4-sized (210 $\times$ 297 $\times$ 1 mm) sensor comprising an optical fiber and silicone rubber. Strain responses in various sensor designs were simulated using finite element analysis (FEA) to safeguard 28 fiber Bragg gratings distributed along the single-core fiber. The simulated environment was further utilized to approximate sensor shape based on finite ground truths, where sparse 3-D positions were enriched to a denser nodes array used. An ensemble learning model that utilized fiber strains as inputs and nodal displacements as outputs were validated with 2.28 mm RMSe at 100 Hz. The hybrid modeling approach was further generalized to a shape sensing framework in a following study. A self-contained optical waveguide sensor was developed on top of optomechanical simulations. Light transmission from simple embedded light-emitting diodes (LEDs) and photodetectors (PDs) was analyzed in advance of modeling. The spatiotemporal characteristic in light intensity variations (input) and 3-D nodal displacements (output) was regarded in an autoregressive model. Underwater experiments demonstrated by a fish-liked shape sensor showcased enhanced prediction accuracy of RMSe 0.27 mm. Real-time shape detection was verified at a update frequency of 150 Hz.

(358 words)

Intelligent Soft Shape Sensing from Sparse to Dense in Real Time

by

MAK Chi Hin

BEng. *HKU*

A Thesis Submitted in Partial Fulfilment

of the Requirements for the Degree of

Master of Philosophy

at

The University of Hong Kong

August, 2023

Acknowledgements

The author would like to express his sincere gratefulness to his parents and life mentors who always stand by for mental support. This work might have stopped in those numerous of failures and never-ending frustration.

To colleagues who learn, share and improve in this research journey, this is the greatest luck in life to work with you all. In particular, the author would like to give his deepest thanks to Dr. Kui Wang, Mrs. Yingqi Li, Mr. Mengjie Wu, Mr. Justin Ho, Mr. Liam He, Mr. Alan Tang, Mr. Chris Tong, Mr. Owen Ng, Dr. Xiaomei Wang, Mr. Jing Dai and Mrs. Becky Chung.

Most importantly, the author is eternally grateful to his supervisor, Dr Ka-Wai Kwok. These three years have been life-changing for an immature, ignorant young boy with zero knowledge of R&D and who believed that the world was circulating his arrogance. The fruitful experiences that sharpen his skills in technical writing, persuasive verbal presentation and hands-on experiments mean so much to the author. The simulating technical guidance and unceasing monetary support have been the best gift one can ask for in pursuing research studies. Dr. Kwok, you deserve all the credit for cultivating a passionate and dedicated researcher. May GOD bless you and your family.

Last but not least, the author would like to acknowledge his alma mater, The University of Hong Kong for its efficient system, world-class environment and exceptional administrative support.

MAK Chi Hin

The University of Hong Kong

August 7, 2023

Contents

List of Figures

List of Abbreviations

ACF	**A**uto**C**orrelation **F**unction
AI	**A**rtificial **I**ntelligence
AR	**A**uto**R**egressive
CCD	**C**harged-**c**oupled **D**evice
DoF	**D**egree **o**f **F**reedom
EGaIn	**E**utectic **G**allium **I**ndium
EM	**E**lectro**m**agnetic
FBG	**F**iber **B**ragg **G**rating
FE	**F**inite **E**lement
FEA	**F**inite **E**lement **A**nalysis
KNN	**K**- **N**earest **N**eighbor
LED	**L**ight-**E**mitting **D**iodes
MEMS	**M**icro**E**lectro**M**echanical **S**ystems
MLP	**M**ulti**l**ayer **P**erceptron
NEMS	**N**ano**E**lectro**M**echanical **S**ystems
PD	**P**hoto**D**iodes
PDMS	**P**oly**D**i**M**ethyl**S**iloxane
PVDF	**P**oly**V**inyli**D**ene **F**luoride
RNN	**R**ecurrent **N**eural **N**etwork

Chapter 1

Introduction

1.1 Motivation and Objectives

Sensor is indispensable to every control system, detecting and discriminating physical stimuli as close loop feedback. Research in intelligent sensors has extended its focus from conventional rigid elements to flexible or even deformable ones. Mechanical compliance of these soft mediums can be exploited to obviate low-level sensing, e.g., deformation complies with the object's geometry in grasping. With increased damping and flexibility, soft sensor is much safer to deploy in human-machine interfaces and wearable devices. These attributes and advantages over its rigid counterpart open up opportunities in many applications, including but not limited to proprioception of soft robotics, attachable artificial skin and actuation control of surgical devices. Soft sensing is emerging to capture signals conventionally unchecked and unrealized. However, the accompanied challenges require much more research to explore and resolve. In particular, signal nonlinearity poses complications to analytical modeling. Closed-form solutions might not always exist in the real world, and be sufficiently accurate when significant hysteresis often occurs. Comparatively, data-driven methods that utilize empirical approximations could represent dynamic responses without much deviation if a proper mapping had been established. Therefore, knowledge of

the targeted system and its sensing response is crucial to determine what and how a model is built. The rationale justifying model selection and model architecture should be problem-descriptive and self-explanatory rather than outcome-based.

In this work, model training data revolves around 3-D morphological changes of a soft sensor during continuous deformation. Processing such high dimensional data entails innovations in both sensor design and learning models, which gather interest in multi-discipline research. This thesis aims to address research gaps and challenges commonly confronted in soft sensor development by investigating a specialized machine learning-based design framework for 3-D morphology sensing. In particular, the form factor of all our prototypes is generally larger than the typical soft sensor without using overwhelming number of transducers and compromising sensing performance. Portability and cost-effectiveness are also considered when compared against some of the state-of-the-art innovations. The integration of computational mechanics and deep learning towards the problem nature of shape sensing is also rarely reported previously. On the whole, the primary contributions are summarized as follows:

1. Design of a large-scale (210 $\times$ 297 mm) surface shape sensor with fiber Bragg gratings(FBGs) and its simulated environment used for design optimization and data enrichment.

2. Design of a self-contained optical waveguide sensor capable of tracking morphological changes, which was validated by optomechanical simulation. Ordinary off-shelf light-emitting devices(LEDs) and photodiodes(PDs) were used as local transducers and multiplexed through wireless communication.

3. Development of a data-driven shape sensing framework based on finite element analysis and deep learning model.

4. Experimental validation of proposed shape sensors and their implemented artificial intelligence(AI) models in various environmental circumstances. Model performance was evaluated regarding accuracy, repeatability, hysteresis and update frequency.

1.2 Outline

This work begins with a review of the recent development of soft sensing systems, and illustrates how it shed insights on prototyping two soft shape sensors. The detailed organized structure is stated as follows:

Chapter 2 presents the rationale for developing a real-time soft sensing system with upfront examples in flexible electronics and optical-based sensing. Crucial advances in prior arts will be covered in terms of their sensing principle, material compliance and overall performance, accompanied by limitations toward a promising solution. The final section summarises and addresses the emerging demand in processing sensing feedback, thus introducing how the integration of computational analysis with a machine learning-based approach may help.

Chapter 3 presents a flexible, thin, A4-sized (210mm $\times$ 297 mm $\times$ 1mm) shape sensor capable of reconstructing high-order deformation in high frequency (100 Hz). Finite element analysis is extensively utilized for sensor design optimization and data enrichment. This Chapter aims to introduce a data-driven modeling framework that takes advantage of computational analysis and ensembling learning. Experimental validation is supplemented to demonstrate sensor robustness as a whole, in particular its capability underwater.

Chapter 4 presents a self-contained, soft optical waveguide sensor capable of reconstructing undulating swimming motion, empowered by an autoregressive model that regards spatial-temporal features in shape sensing. Light intensities data captured by off-shelf electronics (LED, PD) are mapped with 3-D kinematics ground truths enriched by finite element analysis(FEA). As an extended study of **Chapter 3**, optomechanical simulation is incorporated to validate the repeatability of waveguide sensing on top of optimizing sensor design parameterization. The rationale for building an appropriate AI model for high-dimensional time-series data is also discussed.

Chapter 5 concludes the thesis inclusively with all achievements and potential research possibilities.

1.3 Publications

The study is further expounded on the following publications:

1. K. Wang, C.H. Mak, J.D.L. Ho, Z. Liu, K.Y. Sze, K.K.Y. Wong, K. Althoefer, Y.H. Liu, T. Fukuda, K.W. Kwok, “Large-scale surface shape sensing with learning-based computational mechanics,” **Advanced Intelligent Systems**, 2100089, 2021

2. C.H. Mak, Y. Li, K. Wang, M. Wu, J.D.L. Ho, Q. Dou, K.Y. Sze, K. Althoefer, K.W. Kwok, "Intelligent Shape Decoding of a Soft Optical Waveguide Sensor," **Advanced Intelligent Systems**, 2300082, 2023

1.4 Invention Patent

The novel waveguide sensing framework is further protected by the following patent:

1. K.W. Kwok, K. Wang, C.H. Mak, Z.Y. Liu, J.D.L. Ho, "Optical soft skin system for multimodal sensing", **PCT:** PCT/CN2021/128342 [Filed on 3 Nov 2021]; **CPA:** CN116472439A [Published on 5 Jul 2023].

Chapter 2

Real-Time Soft Sensing Systems

The proliferation of soft sensing research in recent years has accelerated breakthroughs in multiple disciplines, including but not limited to artificial skin, wearable devices, soft robots and surgical manipulators. Thanks to its mechanical compliance unfound in rigid sensors, the soft sensor becomes an exciting interface that connects a person to a machine, system, or device. A few decades before, muscle contraction and continuous kinematics of octopus tentacles had never been realized since the conventional sensing approach could barely acknowledge how flexible bodies deform and displace. The beauty of water jetting from elephant trunks, efficient wing flapping of hummingbirds, and all locomotion one can conceive are not skeleton-based behaviors. Only rough estimation can be formulated and utilized in system integration based on discrete sensing feedback. Our knowledge about the physical world is limited without reliable data acquisition and accurate sensing signals. Therefore, reviewing the motivation, capability, and limitation of upfront soft sensors over their rigid counterpart is the first and most crucial step to understanding the direction of the next-generation soft sensing system. The following sessions summarize soft sensors that capture information from mechanical stimuli. Signals, including pressure, strain, or shape changes are discussed.

2.1 Advances in flexible electronics

The use of flexible electronics accounts for a significant portion of soft sensing, where many research efforts are transiting from the integration of micro-electromechanical systems(MEMS) and nano-electromechanical systems(NEMS) with soft medium to a monolithic flexible substrate. From maturely established transducers and receptors to advanced conductive materials, electrical signals featuring high bandwidth and sensitivity have been further enhanced regarding stretchability, scalability, linearity, etc.

2.1.1 Axial Strain and Pressure Sensing

Pressure sensor measures the force exerted on the attached body, with each transducer concerning only a tiny sensing region. In general, multiple smartly arranged transducers are used in a pressure sensor to capture pressure changes over a sufficiently large area. Therefore, the capability of a pressure sensor is often governed by the transducers' sensitivity and spatial distribution.

In some flexible MEMS, pressure transducers and other supplementary electronics are encased by a soft medium. The integration is often characterized by high sensitivity and bandwidth, taking advantage of the established industrial-grade transducers. Cheng *et al.* [1] proposed an elastomer-based robotic skin for humanoid robots by wirelessly connecting thousands of multi-modal tactile modules, each of which comprises an off-shelf proximity and pressure transducer as shown in Figure 2.1**(a)**. In robotic research, these marketable transducers' intrinsic spatial and temporal resolution are sufficient for developing proprioceptive touch sensation. However, the finite size of the pressure transducer and PCB is not favorable for flexible deployments [2], and the rigidity of MEMS inherently restricts its use for complicated motion and body requiring a small bending radius .

Despite the flexibility of the transducer, the flexibility of wiring interconnects is of equivalent significance. Lee *et al.* [3] presented a soft sensing platform that aims to mimic the human somatosensory system with breakthroughs in signal transmission protocol. It enables the use of a larger transducer array (>10,000 pressure transducer) without compromising readout latencies (1 ms) and temporal precision (<60 ns). These resistive transducers are fabricated via a soft lithography process, and subsequently assembled with rigid PCB board (8 mm x 8mm) and flexible interconnects as shown in Figure 2.1**(b)**. This hardware combination slightly improves from the previous modular structure, where deployment on a curved soft body with an irregular shape becomes possible, yet with limited resolution and dimensionality. It fails to differentiate force direction and classify any further stimuli, for instance, orthogonal pressing/pinching and in-plane slipping. As for larger targets, the asynchronous transmission method does push forward the scalability of soft sensing. The burden on configuring sensor design with stable signaling is partly shifted from hardware consideration to algorithm. It shed lights on subsequent sensor development, including this study, to bypass many struggles and repetitive trial-and-error prototyping processes.

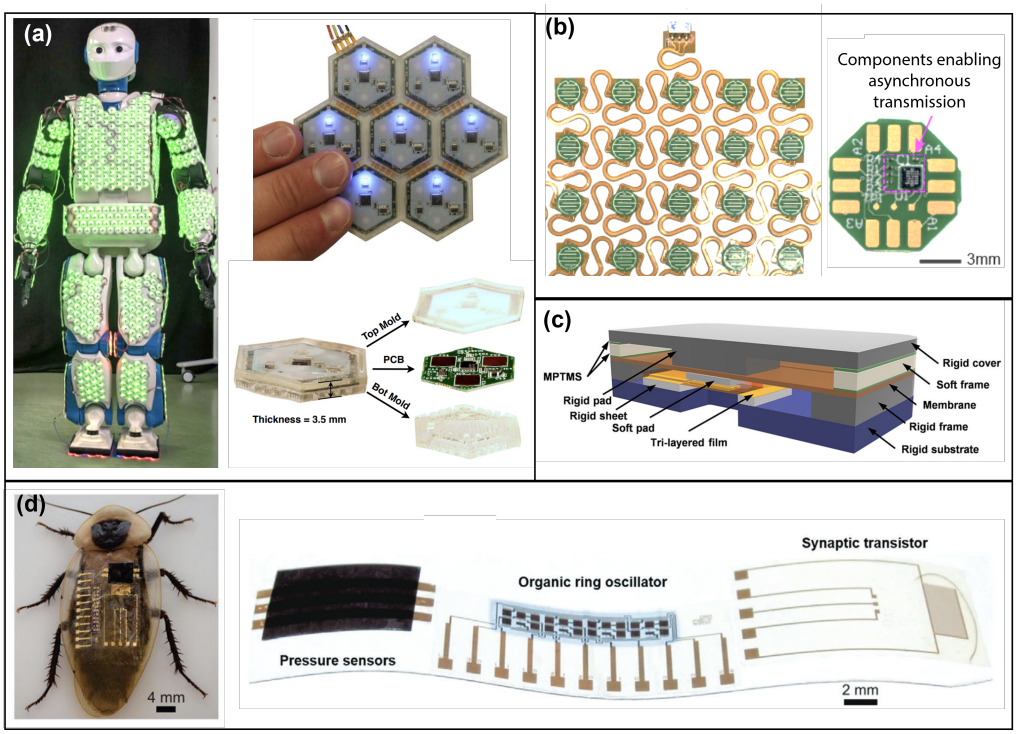

Figure 2.1. Examples of the hybrid pressure sensing system. **(a)** Modular robotic skin designed for large-scale humanoid robot perception, which consists of a PCB-mounted pressure sensor and silicone encapsulation. **(b)** Resistive transducer array mounted on a rigid PCB board (8 mm x 8mm) and connected by flexible serpentine interconnects. **(c)** Schematic of a wireless pressure sensor designed to be hybrid (soft and hard) for injury monitoring. **(d)** Resistive pressure sensor designed to mimic the afferent nerve system. Image Source: [1], [3]–[6]

In view of irreducible rigidity in MEMS, advances in flexible functional material showcase many interesting prepositions in soft sensing [7]–[9]. The simplest configuration of a monolithic transducer comprises a sensory layer, sandwiched by two unresponsive substrate layers. Instead of making a conductive material soft, efforts often put on making a flexible material conductive, by synthesizing electrically active particles in an elastomer. The elastic modulus of the resulting entangled conductive composite network is generally larger than the substrate layer, enabling flexible out-of-plane deformation as a continuous monolithic body (Figure 2.2). One of the most promising electrode candidates, carbon nanocomposites usually contribute a

certain level of stiffness to the sensory layer with elastic modulus > 0.5 TPa, while that of the silicone layer is usually <1,000 kPa [10]. These functional materials can be categorized by working principles as capacitive, piezoelectric, piezoresistive, triboelectric, iontronic and magnetic types. Through nano/microstructure engineering and top-notched fabrication methods, the soft sensor can exhibit various kinds of properties. Some pioneering research efforts are comparable to, or even outperforming the conventional pressure sensor.

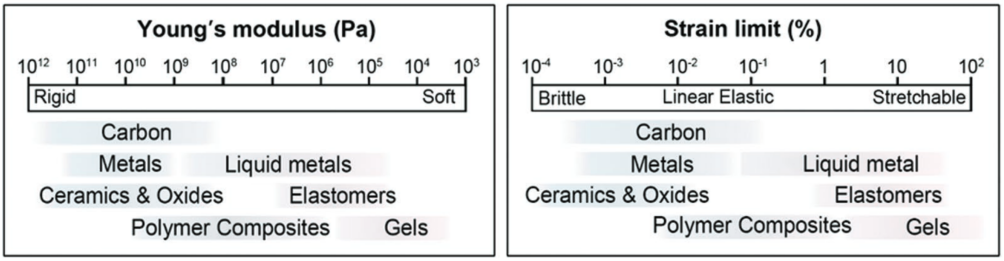

Figure 2.2. Elastic modulus and strain limit of materials commonly used in soft sensing. Image Source: [10]

A recent achievement from Wu *et al.* [11] demonstrated a tactile skin with a novel engineering material Co-based amorphous wire illustrated in Figure 2.3**(a)**, which makes use of the "giant magneto-impedance effect" . During subtle pressure (<1 Pa), a silicone polydimethylsiloxane (PDMS) layer with embedded magnetic particles deforms, resulting in small changes in the magnetic field. Consequently, the impedance of this material vastly increases. Experimental validation shows that the tactile skin exhibits high sensitivity (4.4 kPa^{-1}) in case of a very small loading and contact area (0.5 mN on 40 mm^2), which is beyond the human sense of touch (1 mN). The author suggested the potential for its use in smart prosthetics, but the real integration seems to be distant without any substantial verification. Upon in-depth integration, sensitivity is one of the many performance indices to be evaluated, and more analytical exploration should be discussed.

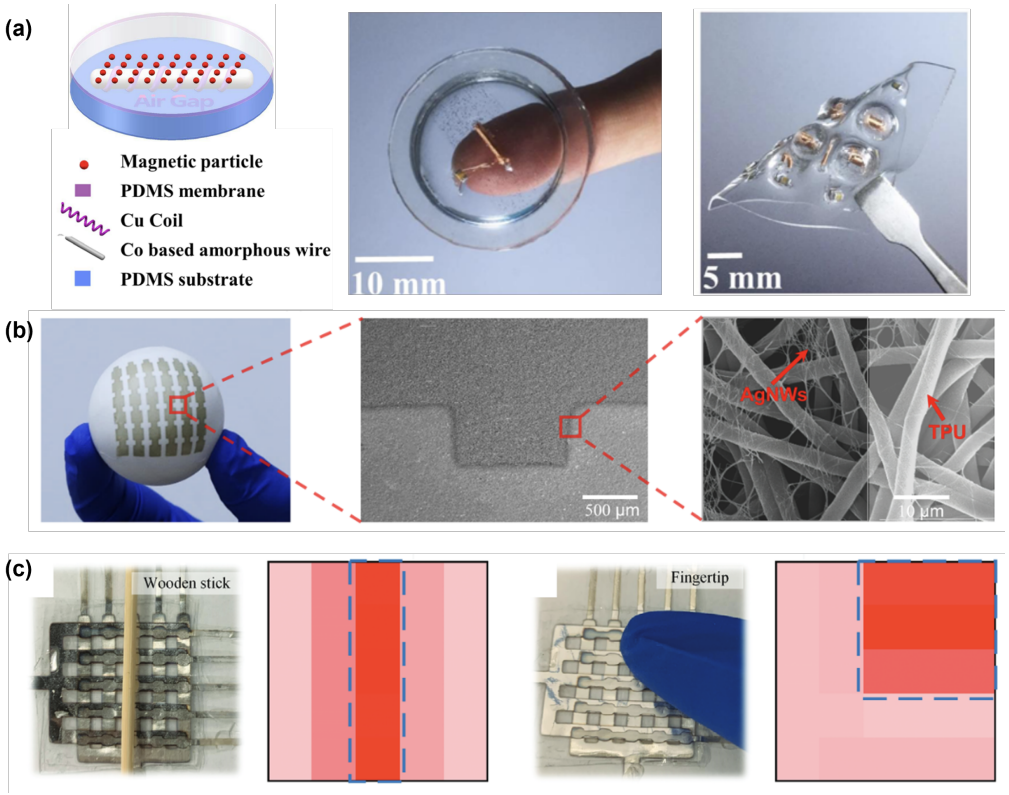

Figure 2.3. Examples of advanced flexible electronics. **(a)** Pressure sensor using giant magneto-impedance effect, where small deformation leads to massive impedance variations. **(b)** Capacitive skin built from layers of silver nanowire and dielectric polyurethane, endowed with ultrahigh sensitivity and low detection limit. **(c)** Polymeric tactile sensor array made by PVDF and PDMS layers detecting the weight of a wooden stick and pressure from the fingertip. Image Source: [11]–[13]

For example, Yu *et al.* [12] proposed a capacitive skin comprising of the silver nanowire (AgNW)-based electrode arrays and two dielectric polyurethane (TPU) layers. Both the grid-patterned electrode arrays and the fabric material are flexible by nature as shown in Figure 2.3**(b)**, and the assembled structure is capable of simple bending, twisting and stretching. The ultra-thin soft sensor($\approx$ 36μm) is breathable and naturally conformable to human skin, while also exhibiting an exceptionally low detection limit (0.5 Pa) and ultra-high sensitivity (8.31 kPa^{-1} under 1 kPa). This breakthrough in permeability is a step forward for an application such as a wearable device,

with essential experimental validation of on-skin deployment. Fingertip pressure over a curved surface was acknowledged, as well as fundamental throat muscle activity detection. The enhanced sensing capability comes with a cost of update frequency (<4 Hz), which may fall short of the requirement in real-time sensing system.

A more responsive piezoelectric pressure sensor by Lin *et al.* [12] utilized two polyvinylidene fluoride (PVDF) films and PDMS layers as shown in Figure 2.3**(c)**. Repeatability test was carried out for 80 000 cycles under a normal force of an amplitude of 15N and frequency of 30 Hz. To further mimic human skin, the sensitivity of this polymeric configuration was optimized by finite-element analysis by adjusting layer thicknesses, similar to that in human fingertips and palms. The optimal sensitivity can reach up to 0.007 VkPa^{-1}, which is possible to detect the take-off and landing movement of a 5 mg spider. However, a spatial resolution of $\approx$5cm^2 is not convincing to be migrated as wearable devices or any other application. The primary parameter contributing to such low resolution is probably the finite size of each transducing grid. One possible resolution is to reduce the size of each transducer and represent the equivalent area with a higher array density, which may be hindered by the prototyping process and technology.

Another challenge in scaling up density and increasing spatial resolution is the electromagnetic interference between each transducer, often regarded as "crosstalk ". Noises stemming from this phenomenon inevitably escalate when more and more transducers are used and closely arranged. It also explains why most soft pressure sensors are not experimentally validated on stimuli over a large area without compromising other performance indexes, such as bandwidth and temporal stability. More critically, soft pressure sensors are transducing mechanical energy over a defined area, implying that the 2-D/3-D force is only represented by a single value. The aggregated pressure matrix is

basically an approximation of the full picture. The continuous pressure profile becomes a discrete representation with a lower dimension than the original stimuli, and the loss of information is eternally unknown and unutilized. Regarding a dynamically varying pressure acting on a soft body (e.g. touch and rub your skin cyclically in natural frequency), current sensing technology fails to capture inclusively all dimensions of the stimuli.

2.1.2 Higher-Dimensional Soft Strain Sensor

To scale up the dimensionality of soft sensing without comprising its performance and maintaining sufficient flexibility for potential application, sensor designs that aim to detect high-level input are discussed. One strategy is to deduce curvature and deformation from the raw impedance variations. Inferring by the classical beam theory, the deformation of the curvature sensor is formulated and computed.

The hypothesis suggested by Liu *et al.* [14] is under small-scale deformation, there do not exist significant differences between beam bending and soft sensor bending. If strains are lengthwise and repeatedly follow a relationship with electrical signals, then using the analytical model is not problematic. Demonstration using a typical strain gauge showed that the mapping from resistance changes to curvature is consistent with the theoretical prediction. A simple bending setup shows that the bidirectional curvature of deployed body can be deduced quantitatively with a GF of 1.5 (Figure 2.4). In case of elastomeric sensors without perfect strain-stress relationship and non-linear deformation, the experimental results deviate from theoretical values The errors that arise from the deformability of soft substrate are significant, and not viable for any application purposes. Similar idea [15], [16] are also used in electrical impedance tomography-based sensing, where pressure signals are used to deduce morphological changes near electrodes.

This indirect deduction inevitably leads to a larger sensing error, e.g., up to 3% [17] in a recent research.

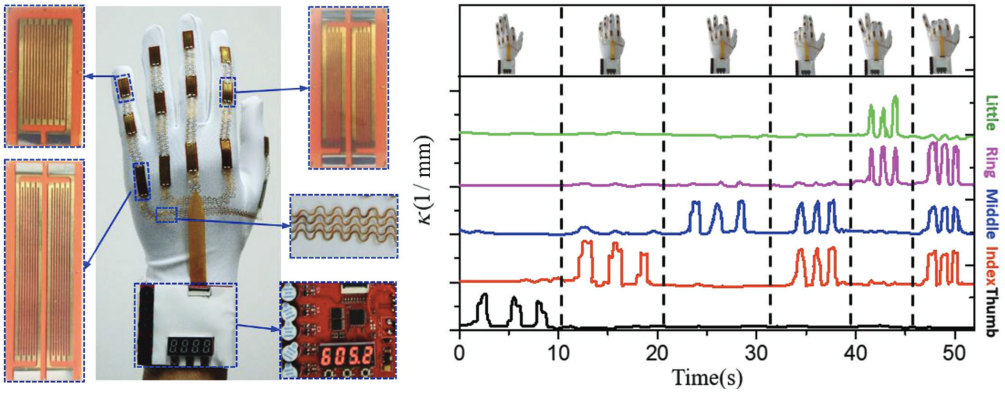

Figure 2.4. Flexible strain gauge-based curvature sensor modeled on classical beam theory. Consistent curvature-strain behavior can be multiplexed when detecting finger bending. Image source: [14]

Different from aforementioned laminating multiple material layers, a monolithic alternative is injecting conductive liquid in a soft medium. The concept is inspired by microfluidics research [18], [19], where inkjet printing technology emerged in the last few decades . In principle, the liquid flows within the closed microchannel without any restrictions, and thus deforming the substrate would inevitably influence the continuous liquid flow. The resulting resistive changes are hence being utilized in soft sensing. In general, the overall mechanical compliance and sensor thickness is thoroughly governed by the substrate material, which also implies more freedom in material choices.

For example, Park *et al.* [20] made a revolutionary attempt by injecting resistive liquid eutectic gallium indium (EGaIn) in a pre-determined microfluidic cavity in silicone as shown in Figure 2.5**(a)**. When the entire soft substrate elongates or compresses, the resulting strains are computed to variations in resistance. By alternating these cavities and stacking layers, multi-axial tactile information can be captured with strain up to 250%.

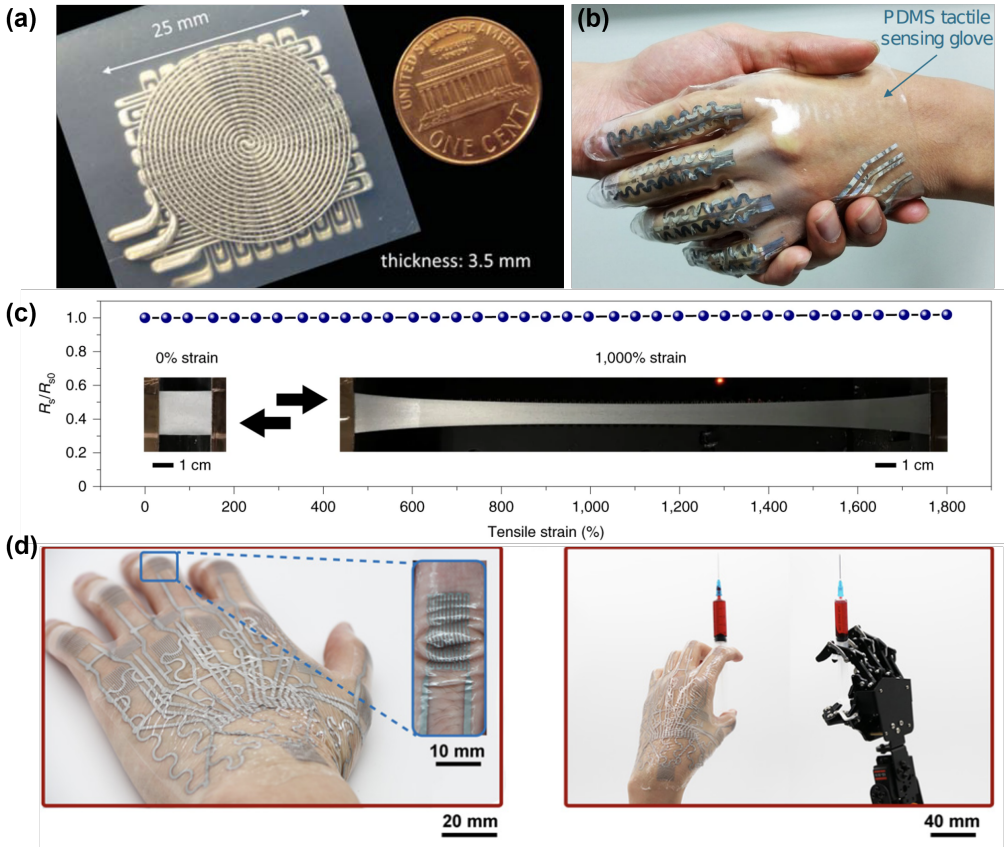

Figure 2.5. Examples of liquid-metal-based soft sensors. **(a)** Three layers of elastomer matrix filled with conductive liquid metal EGaln, capable of sensing bidirectional stretching and pressing. **(b)** EGaIn sensor used as a sensing glove, to detect strains in handshaking. **(c)** Stretchable EGaIn-based conductors that are linearly active to tensile strain up to 1000%. **(d)** Shape-adaptive EGaIn-based tattoo that conforms to the creases of finger joints, which also enhanced strain sensing. Image source: [20]–[23]

Comparatively, it seems impossible to utilize multiple pressure sensors at the same time to capture multi-dimensional information. Moreover, the large strain limit and high stretchability [24] surpass many pressure sensors at that time, and are preferably suited for scenarios with larger deformation . The capability and inherent flexibility of this strain sensor open up new opportunities in soft stretchable sensor, and has shed light on many prototypes thereafter. In some recent breakthroughs in printing technology and the introduction of novel conductors, the ultimate configuration can even

withstand an even higher strain [25]–[27]. Excellent electrical stability is shown with an almost linear strain-resistance relationship in the full ultra-stretchable range, with additional characteristics like high permeability or self-healing ability .

Besides researching sensors and transducing elements, the sensor array arrangement also draws attention [28], [29]. The concept is inspired by "Kirigami", which refers to the Japanese traditional paper-cutting technique that structurally transforms a planar material into a highly flexible hinges-based shape. Conventionally, the grid-based sensor arrangement and the injecting cavity for fluidic conductors are fixed, as well as the equivalent distance between each sensor. The underlying unrealistic assumption is that the deployed body or external stimuli are regularly shaped. Though being claimed as flexible, some of these soft sensors often confront challenges in adaptively conforming to an irregular body shape. Concerning shape conformality, Jiang *et al.* [30] proposed a Kirigami-based capacitive skin that mimics the shape-adaptive ability of snakeskin, conceptually illustrated in Figure 2.6**(a)**. The capacitive sensor array is initially placed on top of a rigid polyimide sheet, followed by a programmable cutting pattern based on required curvilinearity. The cut-out sheet is then linked up by soft conductive hinges for circuit connection. The configuration was verified on rigid cylindrical, saddle, spherical and wavy surfaces. Thus, it becomes possible to deduce strain given from a 3D body when the sensor is guaranteed to be thoroughly shape-adaptive. It should be noted that the sensing capability is derived from cutting pattern adjustment, and the structural stiffness and stretchability are controlled regardless of the transducer used. It implies that the Kirigami technique is supplementary to other advances in flexible electronics [31]. In addition, the sub-millimeter scale cutting pattern can be engineered in finer resolution, similar to how micro-structured pyramids and

domes have been developed to nano-scale [32], and further improve sensor sensitivity .

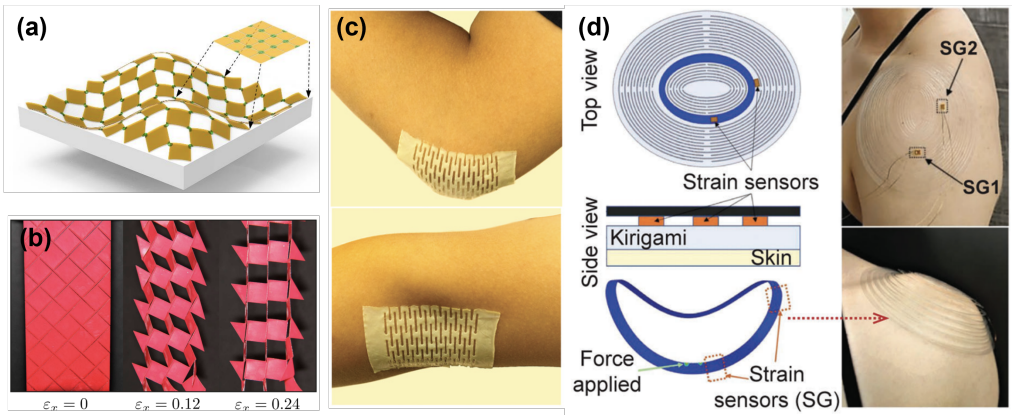

Figure 2.6. Example of Kirigami research in shape-adaptation. **(a)** Soft hinges-linked polyimide sheet with capacitive sensors that conformal to an irregular curvy surface. **(b)** Square array of mutually orthogonal cuts leads to an out-of-plane buckling effect under uniaxial tension. **(c)** Stretchable Kirigami pad with multifunctional electronics conforms to elbow bending, and is used for human-machine interfacing. **(d)** Dense cut-out planar PET sheet capable of tracking the angular position of shoulder joints. Image source: [30], [33]–[35]

2.2 Optical-based soft sensing

Aside from transducing mechanical energy directly to electrical signals, optical-based soft sensing captures information from all kinds of light-matter interactions. Including methods that convert a tactile input into an electrical output using light as an intermediate, and using cameras that track the kinematics of a soft body. This session briefly introduces the core principle and limitations of recent research focus on optical-based soft sensing.

2.2.1 Vision-Based Sensing

A vision-based tracking system is usually installed with a distance from the target objects externally. Many of these market-available technologies rely on the use of markers, often infrared-reflective. Due to the advances in camera

technology and imaging in the last few decades, advanced vision-based sensing of high spatial resolution (< 0.5 mm) and low temporal latency (< 5 ms) have been utilized for dynamic motion tracking (>100 fps). The only but critical disadvantage of this cutting-edge technology, also the reason why it is not welcomed in many disciplines is the line-of-sight dependence [36], [37]. In many health monitoring applications, such as long-term prosthetic devices, external installation [38] goes against the purpose of portable use. To eliminate the problem of line-of-sight dependence, some researches integrate and bundle the camera module with soft medium [39], [40], hence study the image changes as a feedback of displacement or strain.. One representative example [41] was developed by mimicking the epidermis in human skin, where 3-D surface indentation could be mapped into unique representation of light distortion (both magnitude and location) per pixel. With advanced image processing techniques and deep learning models, recent vision-based sensor demonstrate a spatial resolution of 0.4 mm, tactile force accuracy of 0.03 N over a conical finger-like body. The self-contained configuration also enable integration with soft actuator of similar shape, however, may bulk up the overall form factor and hinder application in narrow workspace. The portability comes with the expense of bulkiness as well as a finite, bundled volume of rigid components, which may further limit its potential usage in case of a larger scale of deformation.

2.2.2 Fiber Optics

Owing to the advances in photonics and the demand for long-range telecommunication, the technology of fiber optics has been maturely established in the last few decades. Typically, optical fiber is a more flexible waveguide option than vision-based device, where the core medium is surrounded by a cladding medium with a lower refraction index. With proper

material choices, light can be kept in the core with minimum propagation loss according to the principle of total internal reflection. Most importantly, optical waveguide materials are usually endowed with flexibility, where optical fiber can be used in a standalone configuration or attached to a soft substrate.

In general, optical fiber sensors can exhibit high sensitivities to external physical perturbations such as temperature, strain, acoustic vibration, current, pressure, etc., that can surpass other existing techniques by tens to a hundred decibels in sensitivity in some cases. The immunity of silica optical fiber to electromagnetic interference and resistance to high temperatures and corrosive substances allows optical fiber sensors to be used in various harsh environments [42]. Furthermore, the compact fiber geometry, flexibility, and light weight of optical fibers provide a very high degree of freedom in applications with limited space and portability requirements. Optical fiber sensors are point-wise sensors distributed in an array along the fiber length, which can be multiplexed using a single light source and detection system. Current distributed sensing technology utilizes two types of light scattering to sense strain, namely Rayleigh and Brillouin scattering [43]. The scattered light carries the information of intensity loss during propagation due to the variation in the refractive index. In case of curvature changes or local pressure at any location of the optical fiber, the refractive index of the cladding material at the relevant region will be affected, as well as light propagation. Depending on the required spatial resolution, accuracy and fiber length, the interrogation technique can be specifically selected in terms of scattering method and multiplexing arrangements. For instance, optical frequency domain reflectometry (OFDR) utilizes Rayleigh scattering and receives a frequency response from the optical fiber [44]. Using Fourier transform, strain sensing can be almost perfectly linear with high strain accuracy $1\mu\epsilon$. However, the bottleneck of data acquisition frequency (ranges from mHz to Hz) is not

eliminated even in the recent demonstrations.

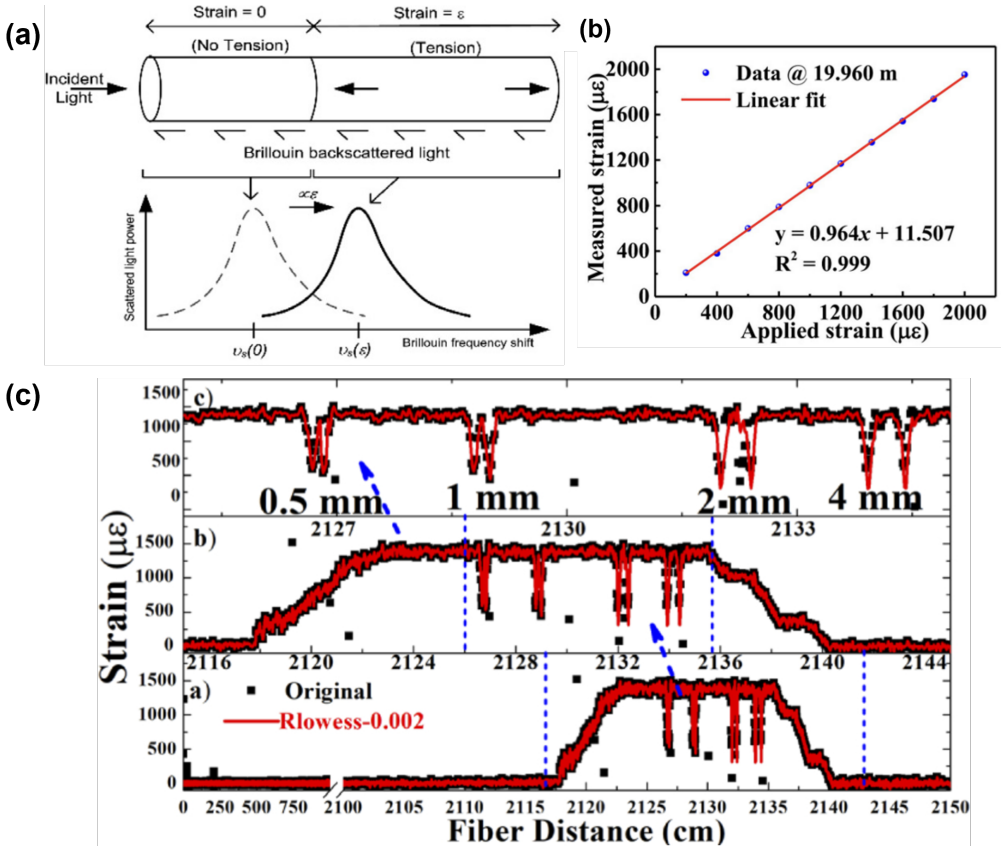

Figure 2.7. **(a)** Frequency shifts of Brillouin backscattered light when subjected to tensile strain. **(b)** Strain-sensing accuracy plot of a recent OFDR strain sensing approach, which enhanced spatial resolution to 2.56mm of a 25m fiber. **(c)** Strain responses of another OFDR distributed sensing of low spatial resolution (0.5mm). Image Source: [43]–[45]

Comparatively, the data acquisition frequency of shape sensors built from micrometer-sized FBGs can reach up to the scale of kHz. It refers to a permanent index modulation at the core of optical fiber in a periodic pattern. The modulated regions, also called fiber Bragg gratings allow the transmission of some wavelengths and reflect others based on their period. When subjected to strain, the grating is mechanically deformed, hence influencing the reflected wavelength. The relationship of all these quantities is thus linked up, and can be mathematically formulated. Recent research has shown how FBGs can be leveraged to reconstruct higher dimensions, such as curvature and 3-D

morphology sensing based on axial strain sensing [46], [47]. One of the implementations employs multicore fiber, a special kind of configuration that embed multiple fiber core with single cladding. When subjected to a longitudinal strain that is proportional to the distance of fiber's neutral axis, the distinct responses of each FBG can be calculated as the local curvature and aggregately approximated as the global shape.

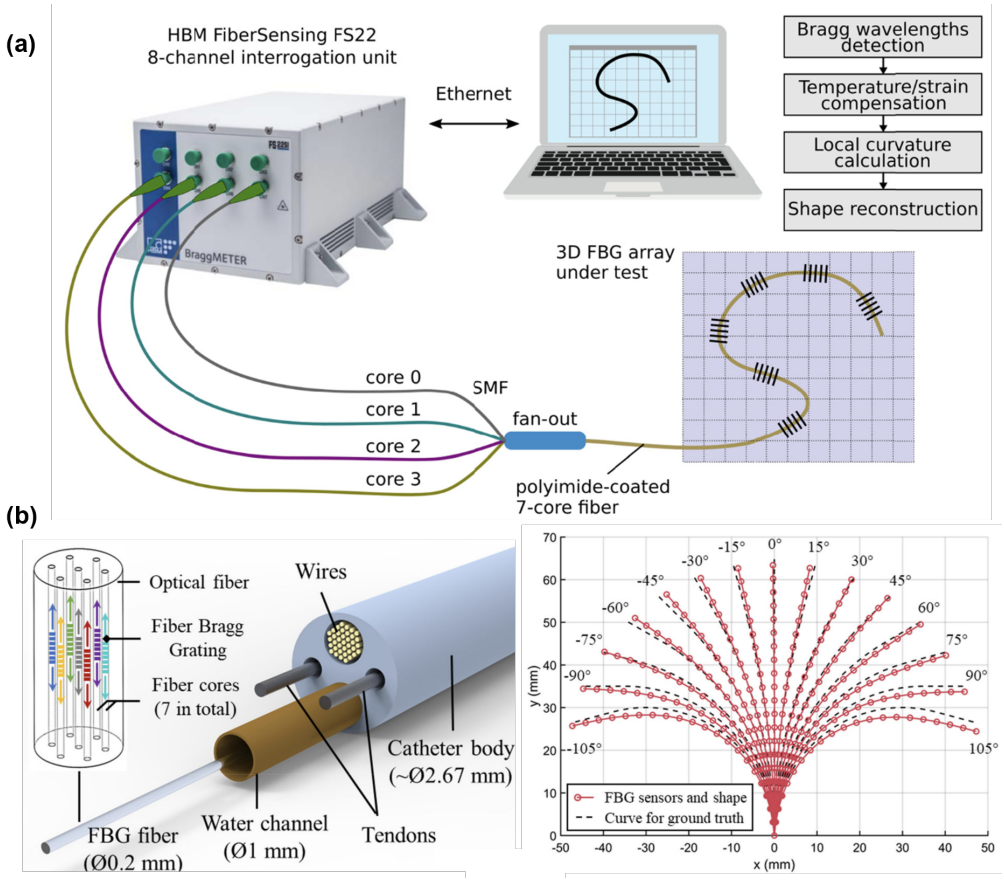

Figure 2.8. Examples of multi-core optical fiber with FBGs. **(a)** Standard experimental set-up for the use of multi-core FBGs in shape sensing. **(b)** (Left) Seven-core FBG fiber placed inside the water channel of a standard electrophysiology catheter. (Right) Shape sensing accuracy in various curvatures for closed-loop robotic control. Image Source: [48], [49]

For example, Dong *et al.* [49] incorporate the shape sensing feedback in their closed-loop control of a robotic cardiac catheter system in Figure 2.8**(b)**. Diameter of 0.2 mm seven-core FBG fiber is placed inside the water channel of

a standard electrophysiology (EP) catheter, tracking the 3-D steering of its distal bending section. Twenty-one FBGs are used for each core to reconstruct the distal catheter section of 63.4 mm in real time. *Ex vivo* experimental validation showed that the average angular error of all FBG sensors is 2.33° and the average positional error of 0.63 mm. In a fluidic environment under a magnetic resonance imaging setting, optical-based soft sensing surpasses any electromagnetic approaches. In addition to the demand for real-time sampling frequency, compact design and high-dimensional feedback, multicore optical fiber with FBGs is groundbreaking. However, the configuration of multicore fiber is often optimized for telecommunication purposes in terms of cladding diameter, core spacing and fiber length. A more cost-effective alternative could be using a more common option, single-core FBGs.

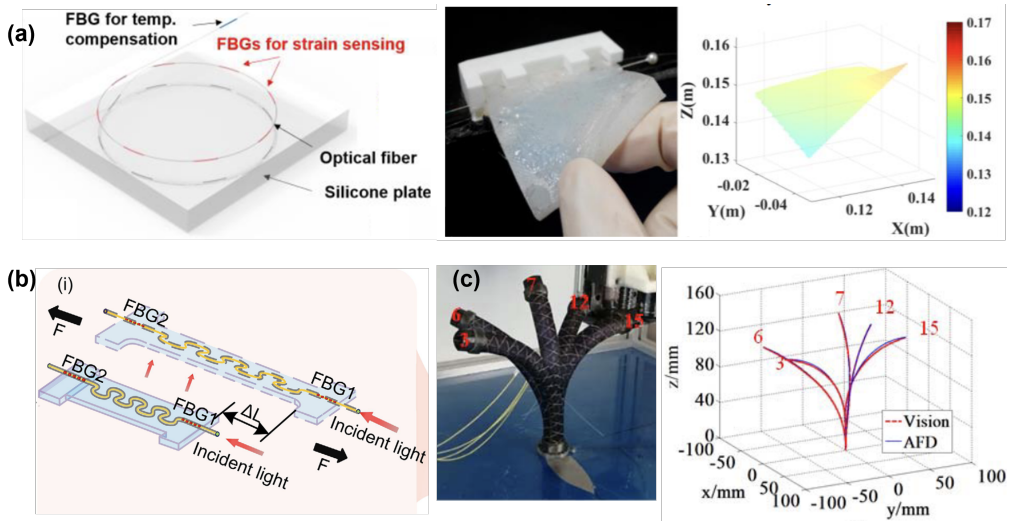

Figure 2.9. Examples of single-core optical fiber with FBGs. **(a)** (Left) FBGs routed circularly at the top and bottom surface of a thick (5mm) shape sensor. (Right) Shape reconstruction performance in real-time (10 Hz) **(b)** Ω-shaped routing of a radius 3 mm that increases detection range of tensile strain by 200%. **(c)** Three optical fibers helically wrapped around a soft manipulator that detect its curvature in a quasi-hemisphere workspace. Image Source: [50]–[52]

In recent research, single-core FBGs have adhered to soft medium in a variety of curvilinear routing layouts to leverage their axial strain detection to a higher dimension [50], [53], [54]. The concept behind this is, to extend the

strain-sensing capability of FBGS from optical fiber segments to a larger area/volume of the flexible body. Though by definition, not a monolithic body, the fabrication errors incurred are mostly negligible to computation. For example, Lun *et al.* [50] made use of two optical fibers with 16 FBGs, circularly routing at the top and bottom surface of a silicone substrate of 45 x 45 x 5mm with silicone epoxy adhesion as shown in Figure 2.9**(a)**. The soft sensor is capable of real-time (10 Hz) reconstructing simple bending based on shallow artificial neural networks. The primitive results suggest the possibility to utilize strain sensing in higher dimensions, although limited by sensor thickness and flexibility. Further exploration of stretchability routed a single optical fiber in a Ω-shaped arrangement of a radius of 3 mm [51] in Figure 2.9**(b)**. The detection range of tensile strain increased by 200%, noting that optical fiber exhibits almost zero stretchability by nature. When attached to the human body, multiple sensors were multiplexed against distinct strain performance from respiratory rate, joint motion, etc [52].

However, the complexity of strain signals in previous examples is rather straightforward, either bounded by the sensor thickness or strain dimensionality (only axial). Such sensing capability can possibly be achieved by flexible electronics with higher flexibility and durability, given that FBGs are exceptionally fragile. A more convincing implementation is reconstructing the curvature changes of a soft actuator in a quasi-hemisphere workspace. The nonlinear deformation of soft silicone rubber (outer diameter 20 mm) was modelled based on FBG-based piecewise constant curvature. Three optical fibers were helically wrapped around the continuum robot with phase difference 120°, and accurately detect the axial elongation/compression during bending. This approach has generated interest in soft robotics research, as optical fibers can be directly integrated into the robot structure to model and reconstruct its behavior [55]–[58]. However, despite the advantages of FBG

fibers, including exceptional thinness (<300 µm), electromagnetic immunity, and multiplexability [43], they still face challenges in terms of relatively rigid fibers, which can inhibit the ultimate sensor flexibility. Additionally, FBG fibers entail high costs and bulky measurement equipment (i.e., optical interrogators) [59], [60].

2.2.3 Waveguide Sensing

One possible approach that omits the use of tethered interrogation while retaining the advantages of fiber optics shape sensing is optical waveguide shape sensing. It refers to the detection of light transmission within an optical waveguide, including but not limited to optical fiber. The core concept of total internal reflection is still regarded, but most likely in other form factors and materials. In particular, advanced materials with higher stretchability and exceptional refractive indices are concerned.

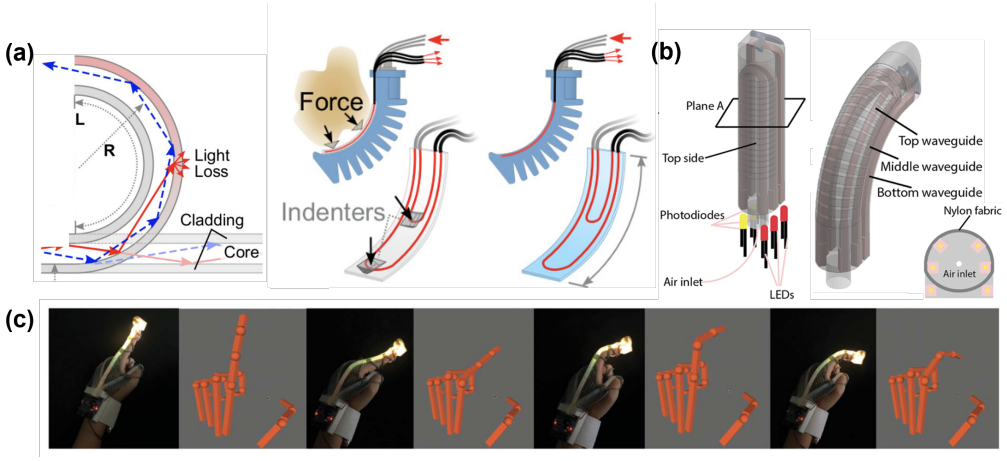

Figure 2.10. Soft waveguide sensing prototypes. **(a)** Intensity loss due to bending was characterized as a function of curvature and local normal force in the waveguide sensing of a soft pneumatic gripper. **(b)** Similar soft finger design with a U-shaped waveguide that uses simple optoelectronics (LEDs and photodiodes) for intensity loss modeling. **(c)** Recent color-based waveguide sensing that enables skeleton-based finger motion reconstruction. Image Source: [61]–[63]

For example, Teeple *et al.* [61] developed a 1 mm thick rectangular optical

waveguide that was attached to a soft pneumatic gripper to track its bending curvature and contact force. Contrary to upholding minimum propagating loss as in optical fibers, deformation is characterized in relationship with light loss. When subjected to deformation, some of the lights fail to follow internal reflection due to curvature changes. Though shape changes might be proportional to strains, the sensing principle of optical waveguide omits all strains-relevant calculations [64]. The experimental intensity loss was then modeled as a function of deformation. The intended use of light loss is also found in other finger-like structures, mostly utilizing simple optoelectronics, namely LED and PDs [65]. The light emission can be coupled with optical silicone rubber (refractive index ≈ 1.4) over the visible light spectrum, nothing that only a narrow range of invisible light ($\approx \pm 10$ nm) is sensitive to FBGs and distributed sensing. The wide range of color (wavelength) sensitivity was utilized in another prototype that bundled two waveguides together. White LED light was transmitted at one waveguide core and lost to another rainbow-dyed waveguide. Based on the color intensities, the finger-like sensor can detect accurately the local deformation and the overall shape changes.

In addition to shape changes, the reduction in light intensity was also used as a state signal in a self-healing soft robot [66]. Similar to previous examples, the light transmission was used for closed-loop control feedback of pneumatic pressure actuation. The soft quadruped robot crawled forward using light losses feedback from each leg, and additionally, continuously detecting structural damages that cut off the waveguide (Figure 2.11). The resulting reduction in absolute light intensity would have stopped the robot until the self-healing effect of the waveguide took place. The idea is not common in electrical-based soft sensors as the conductivity of electrically-active materials might not be 100% self-healed.

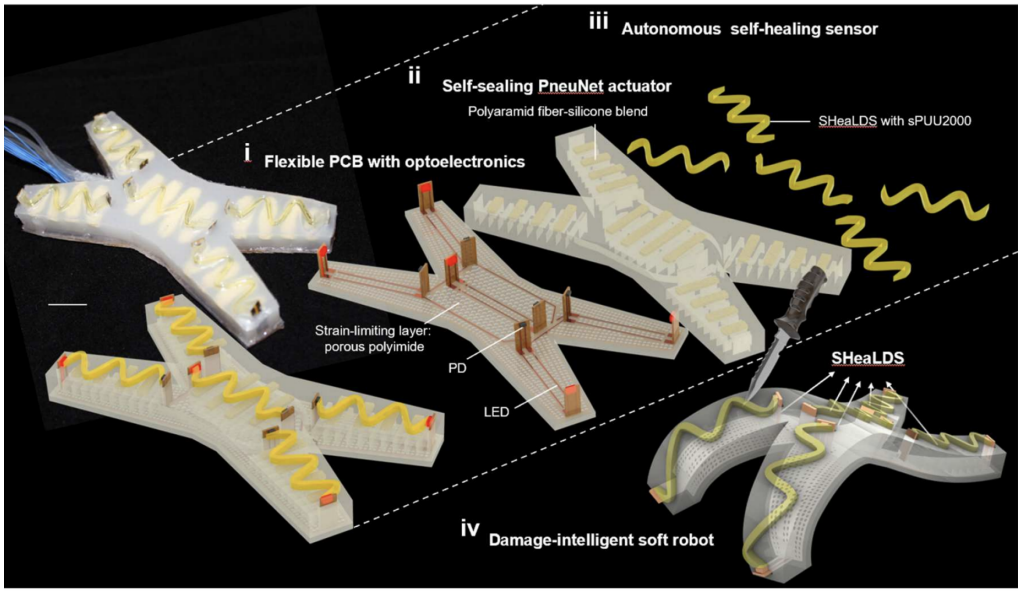

Figure 2.11. Soft self-healing waveguide robot that crawls forward. Five pairs of LED and PD are embedded in the actuators, monitoring the gait and damage state of the quadruped and controlling the movement direction based on the damage condition. Image Source: [66]

2.3 Conclusion

To conclude, this chapter reviews various soft sensors based on their sensing dimensionality and transducing mechanism/ working principle, spanning from rigid MEMS to flexible functional material, liquid metal, FBGS and the optical waveguide. The mechanical compliance of soft materials safeguards a risk-free interaction and collision, which is vital in human-machine interfaces. Based on various applications and integration platforms, the mechanical requirement for soft sensors varies, and entails new challenges for future innovation. Collectively, the soft medium used as encapsulation, dielectric supporting layer and optical waveguide in form factors of a thin substrate, has been a crucial component influencing sensor flexibility. Mechanical properties including Young's modulus, elastic limit (elongation), strain limit (fracture), bending radius and structural stiffness could help quantify soft sensors' flexibility. Further investigation on material properties like biocompatibility,

permeability and adhesiveness also encourages the potential integration into healthcare applications, such as wearable devices and implant devices. Besides a high degree of compliance, an all-rounded strategy that improves the overall user experience has been suggested. The sensing system may incorporate a wireless module and battery (or self-powering ability) instead of implementing a standalone sensing prototype. The elevated structural complexity is often unconsidered in the research stage, but it could be challenging to package everything into a durable, robust body. The advantages of monolithic design, the ease of fabrication, and the cost-effectiveness govern how translatable research efforts can be reliably applied.

More importantly, the emerging demand for a high-performance soft sensor is unmet given mechanical stimuli. Multi-modality and multi-functional characterization often appear to be non-mechanical, such as the capability to sense electrocardiography signals and temperature variations. Pressure and strain sensing thus remains one-dimensional and provide low-level feedbacks, which may still be sufficient to use in scenarios where a simple pressing button is needed. The dedication to elevating signal dimensionality is surging, especially in fields that may not exist any convincing solution, for instance, the proprioception of soft robots. Accompanied by the difficulty in leveraging soft sensing in a higher dimension, the hardware complexity in scaling up the size also requires more research efforts. It is common to conceive that stacking up the amount of transducing units could immediately increase the scale and dimension of sensing. However, upfront research reveals that the enhancement comes at the expense of system stability (crosstalk), bandwidth (temporal latency) and flexibility (physical connection).

The underlying challenge in real-time soft sensing systems can be understood as the difficulty in capturing a vast amount of physical stimuli

changes as well as the processing capability to acknowledge these data with finite computing time. Apart from novel materials and prototyping methods for sensor arrays, simulation is one possible approach to capture an equivalent amount of information with reduced hardware complexity. Assuming high consistency with real soft sensors, virtually generated data are noise-free and almost infinite in amount. In some cases, the iterative computing cost is much smaller than the fabrication cost, given that most research efforts are in an experimental stage with a certain level of failing risk. Once a reliable dataset is generated, data-driven modeling might be one of the best alternatives to explain the relationship between physical stimuli and sensing data. In the latter Chapter 3, simulations of sensor performance are covered in detail to showcase how it can be enhanced by only using raw sensing signals, i.e., FBG strains. Our research explores using neural networks to model the mapping between the simulated data and sensing outcomes. Based on the prototype in Chapter 3 and its experimental results, I extend the work to generalize our sensor design framework with another type of raw data such as light intensity. The overall objective is to demonstrate how a deep learning model can be capable of realizing the mapping from the raw sensing signals to explicit morphology details.

Chapter 3

FE-based Data-driven Shape Sensing Approach

3.1 Introduction

One critical challenge in real-time soft sensing systems is the nonlinearity in soft medium, often brought over by its mechanical compliance. The issue becomes increasingly vital when the sensing area escalates, accompanied by other challenges reviewed in Chapter 2. Apart from soft sensing, modeling and controlling potentially unpredictable behavior of soft materials have also been emerging research questions in soft robots. In particular, the infinite degree of freedom(DoFs) during actuation and interaction with the environments may not have any theoretical formation to describe and model. If required, the unrestricted deformability entails additional complications for their perceptions at locations all over their soft body. This implies a sensing approach that tracks continuous deformation rather than a discrete grid-based sensing array and differential information derived from joint-based kinematics.

To empower soft robots with such sensing capability, this Chapter aims to explore a data-driven modeling approach with shape-sensing FBGs.

Compared with other soft sensors, the advantage above of optical-based sensing and single-core optical fiber is an interesting direction to explore. Without much fabrication complexity, investigation on high-dimensional shape sensing feedback can be initiated and begun using off-shelf optical fiber with FBGs. In some data-driven modeling sensor research, the sensing performance is often limited by the hardware sensor configuration, and fails to demonstrate why a data-driven model is essentially needed. For example, Rendl *et al.* used a nonlinear mapping function that learns the raw measurements from piezoelectric sensors to meshed surfaces [67]. The irregularly distributed sensor array achieved the continuous surface deformations of an A4-sized sheet. However, the sensing accuracy remains at the centimeter level, which was still far from any meaningful application. A more accurate demonstration utilizing optical fibers came with the cost of portability. By integrating the illumination and detection devices, the deformation of silicone rubber was decoded by light loss within 30 regularly distributed optical fibers [68]. The optical feedback was then trained by multiple deep-learning models with the lowest error of 0.06° in the k-nearest neighbors(KNN) method. The KNN model was also used to classify deformation patterns with 100% accuracy, explicitly simple bending and twisting. Though showcasing excellent performance, the modeling approach did not explain any physical phenomenon. Therefore, the proposed data-driven modeling approach in this Chapter aims to describe the raw sensing signals in a step forward to construct a generalized framework for soft sensing. (Figure.1) To begin with, a sensor design capable of high-order morphological changes was investigated.

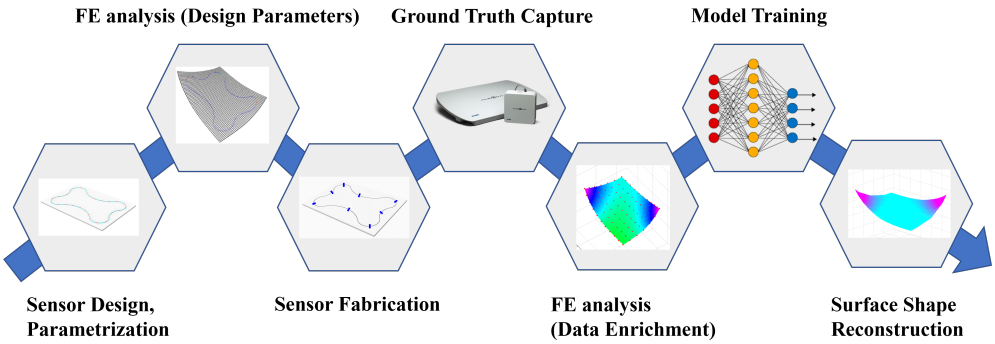

Figure 3.1. Step-by-step workflow of the data-driven modeling approach regardless of shape sensors used.

3.2 FE-based design optimization

Before prototyping the soft sensor comprising the single-core optical fiber and FBGs, iterative simulations were explored to see how sensor design may affect data shapes and training quality. The following pilot study examined the strains of a single optical fiber and its attached silicone rubber under various deformation patterns using FEA. The virtual sensor was set to have equivalent material properties to guarantee the simulation was consistent with the physical prototype.

3.2.1 Simulation settings

Explicitly, the elastic modulus and Poisson's ratio of the silicone is 2.192 MPa and 0.393, respectively; that is 70 GPa and 0.1638 for the optical fiber [69]. These numerical values were determined following the ASTM-D412 standard, using digital image correlation [70], [71]. The testing specimen was stretched at a 10 mm/min uniaxial loading velocity, synchronously recorded by a charge-coupled device(CCD) camera at a frame rate of 10 Hz. Both materials were then set as linear elastic three-dimensional deformable parts. In reality, the stress-strain curve of both silicone and silica optical fiber is not linearly elastic but is sufficiently valid for most deformation patterns. Scenarios

beyond elastic deformation may often approach the breakage limit, and certainly beyond the allowed motion range/workspace, which this thesis would not discuss—further setting up the mesh element into eight-node brick elements (C3D8I) for silicone and two-node linear 3D truss elements (T3D2H) for optical fiber. The incompatible deformation modes setting minimizes unfavorable parasitic shear strains commonly occurring in its fully-integrated alternative (C3D8) and zero-strain deformation in reduced-integration alternative (C3D8R) [72]. The hybrid element mode setting was additionally used to safeguard the incompressibility of FBGs since it is much more fragile than the optical fiber, where volumetric changes of tiny grating periods are equivalent to breakage. Furthermore, the optical fiber was constrained with surface-to-surface contact with the soft medium, ensuring it always conforms to the deformed shape of silicon rubber.

In this initial attempt, a form factor of standard A4-sized (210×297 mm) was selected. It is sufficiently large to illustrate various deformation patterns, especially those irregular, non-primitive shapes. A single-core optical fiber carrying 29 FBGs was used, where 28 were used for strain sensing and the remaining for temperature compensation. This is also a common practice seen in previous research because the gratings are sensitive to temperature changes; thus, keeping a temperature sensor guarantees the measurements are stable [73]. Multiple design considerations were simulated to evaluate how sensor design influences raw strain responses, assuming geometrical nonlinearity may occur. Structural stiffness may vary in large deformation with clamped elements and lead to geometrical changes. A more straightforward example is the little stretching effect when a clamped silicone rubber is bent with large deflections. This effect may be negligible in actual application, but it is significant in the following simulations.

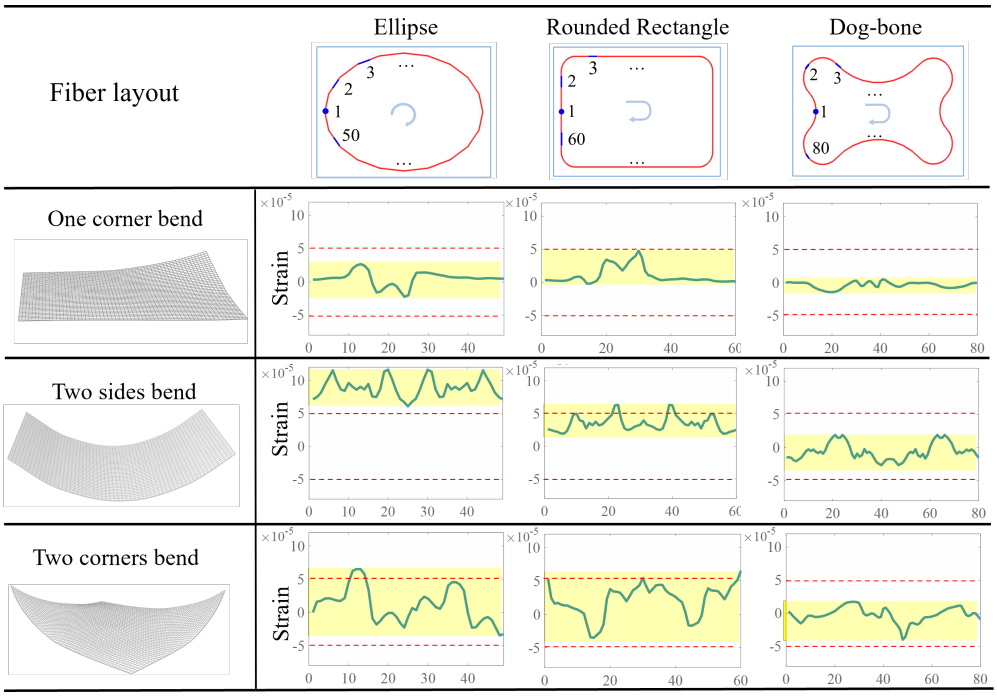

Figure 3.2. Simulated fiber strain responses of three fiber routes subjected to three deformation patterns. The dog-bone-like route has the smallest Peak-to-peak strains (yellow) than the elliptical and rounded rectangle route. With equivalent spacing between FBGs, the total length and number of FBGs used also vary, i.e., ellipse shape is shortest with 50 FBGs

3.2.2 Fiber strain responses

Firstly, the fiber route and the distribution of FBGs were analyzed. The strain responses of three fiber routes undergoing three virtual deformation patterns were simulated as shown in Figure 3.2. A smaller peak-to-peak strain range was demonstrated in the dog-bone-like, implying that the deformation pattern does not exert a significant strain on optical fiber. For those small strains very close to zero, the challenge shifts to the intrinsic sensitivity of FBGs. It is also true to conclude that the small range suggests the potential to undergo more irregular and localized deformations, possibly tears off the fiber if either ellipse or rounded rectangle was used. With reference to optical fiber research **li202**, **2skin**, [50], [52], [57], [67], an ideal route should have evenly distributed the FBGs over the sensing area such that local strains at most possible locations

could be captured and realized. Following this logic, the dog-bone-like route outperforms the other primitive routes by tracking the strain variations in the central region. However, a perfect route is still unknown regardless of the limitation in the amount of FBGs and its spatial resolution (spacing).

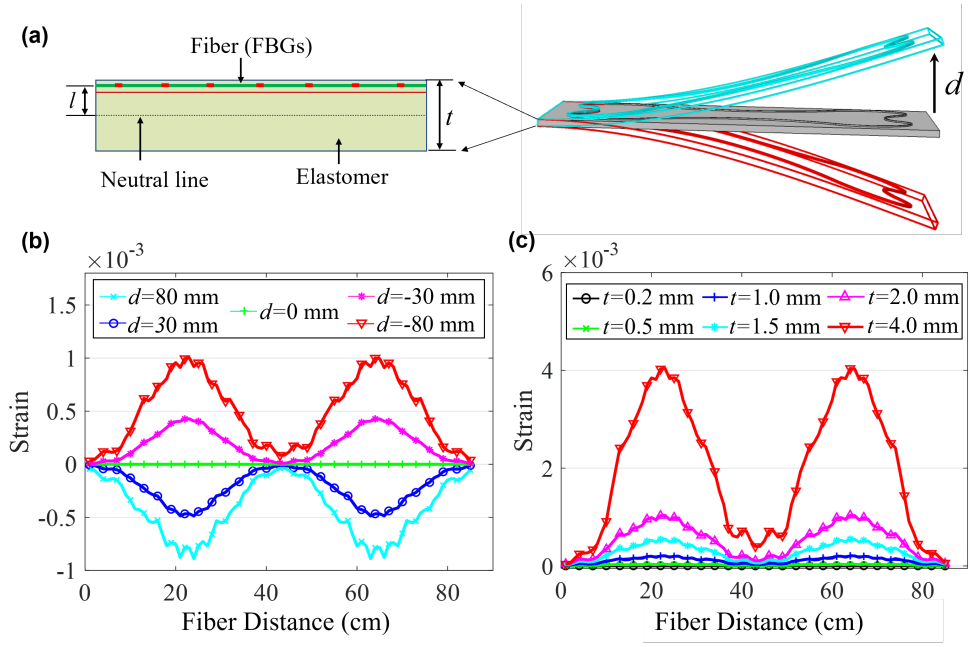

Figure 3.3. Simulated fiber strain responses of various sensor thicknesses. **(a)** Cross-section view of the surface-adhered fiber of total thickness t when subjected to simple bending. **(b)** FBGs strain responses against displacement d within $\pm$80 mm along a optical fiber length(i.e. distal fiber end has the largest fiber distance). **(c)** FBGs strain responses against thickness t range from 0.2 to 4 mm.

The simulation proceeded to the thickness with the dog-bone-like route. Thickness undoubtedly decides how flexible the soft sensor is, and should not be too large. In case of using an optical fiber of diameter 125 µm, the sensor could not be too thin to serve as a protective layer. In the simulation of one-end-clamped bending shown in Figure 3.3, the fiber strains increase with the sensor thickness. The data shape looks similar but the magnitude of fiber strains is more than proportional to thickness. In view of the high sensitivity of FBGs, the absolute strains need not be very high. Based on Kirchhoff plate theory

[74] and related research [50], [75], the distance offset from the mid-plane of bending is also relevant to fiber strains. For simplicity and the bidirectional sensing capability, the sensor design confirmed the 1 mm thickness assuming the optical fiber adhered to the surface of silicone rubber.

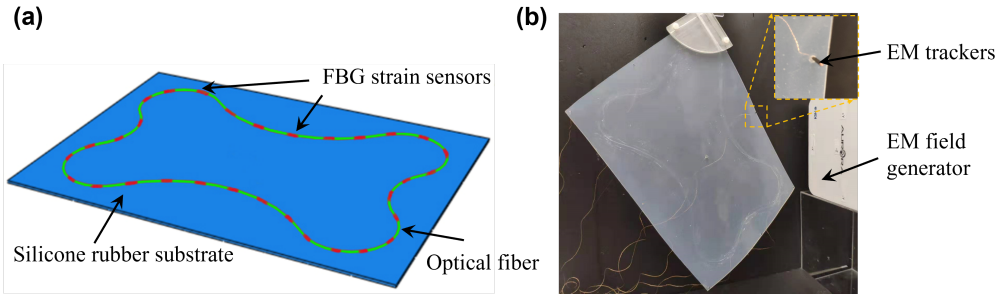

Figure 3.4. **(a)** Large-scale shape sensor prototype (210 × 297 × 1 mm) comprises of an FBGs-carrying optical fiber and a silicone rubber substrate. Sparsely distributed FBGs routed in a dog-bone-like layout targeting the local strains over the continuous soft body. **(b)** Experimental set-up for capturing sensor deformation using electromagnetic (EM) tracking system. Eight EM markers were attached on the rubber substrate.

3.3 Sparse-to-dense data-driven modeling

To realize shape changes of the A4-sized soft sensor (Figure 3.4(a)), the data-driven model should map the fiber strain responses to surface deformation. One of the best alternatives to capture the deformation of soft sensors is electromagnetic(EM) motion tracking system. By attaching EM tracking markers on the sensor surface (Figure 3.4(b)), their 5-DoF values with regard to a confined workspace could be captured. However, it is physically impossible to adhere so many markers all tethered to an interfacing machine, let alone resolve the reduction of sampling rate by multiplexing more markers. The issue of marker adhesion similarly happens to camera-based technology which is bounded by additional line-of-sight dependence. The core obstacle in large-scale shape sensing is uncovered to be an appropriate method that accurately represents the continuous sensor regardless of its deformed shape.

In some previous research efforts, the finite element(FE) model was used as an alternative to interpolation techniques. Thanks to the geometrical and material constraints, the simulation often provides higher accuracy than polynomial-based interpolation. The virtually generated shape is continuous by nature with many output points based on the number of meshed elements. For instance, Lee *et al.* made use of the simulating data to initialize a kinematics model for soft robot control [76]. The iterative simulation came with an expense of high computational cost and limited the use in a nonparametric model. A straightforward resolution is reducing the computation complexity so as to cut down the time cost [77], which may not be feasible in the scope of this thesis. The advances in hardware computing units and parallel computing strategies to date are still insufficient to push forward FE simulation in real-time usage [78]. Nevertheless, the computational cost is not a severe issue if used appropriately in machine learning [79], where the computational time is primarily governed by the complexity of the model. The computation time needed for a trained model is comparatively a few orders below that for FEA [77]. Ultimately, the bandwidth and the sensing frequency could still become a problem and were explored after the discussion in FE data enrichment.

3.3.1 FE-based data enrichment

To verify whether data enrichment could provide a reliable dataset, the ground truths were captured by the EM tracking systems (Aurora® V3, NDI) and input in the previously established simulation environment. Nine EM markers were evenly distributed on the A4-sized silicone rubber to capture the spatial coordinates that were synchronous to FBG strain sensing (FBG-Scan 804D). Various deformation patterns were manually performed over 2 minutes at a 40 Hz sampling rate. The nine control points were then subsequently used as a

boundary condition that transiently confines the motion of the virtual sensor. Eventually, the 3×3 ground truths were enriched to a selection of a denser grid. Compared with bilinear and non-linear interpolations [80], the simulation was more accurate (Figure 3.5). When statically placed over a cylinder of diameter 115 mm, the errors in approximating the continuous surface using 9 query points were beyond acceptable for the interpolation technique. The maximum displacement errors for these methods were 3.2 mm, 19.7 mm and 16.8 mm respectively. Theoretically, using more control points should further lower the error and it is applicable to all methods.

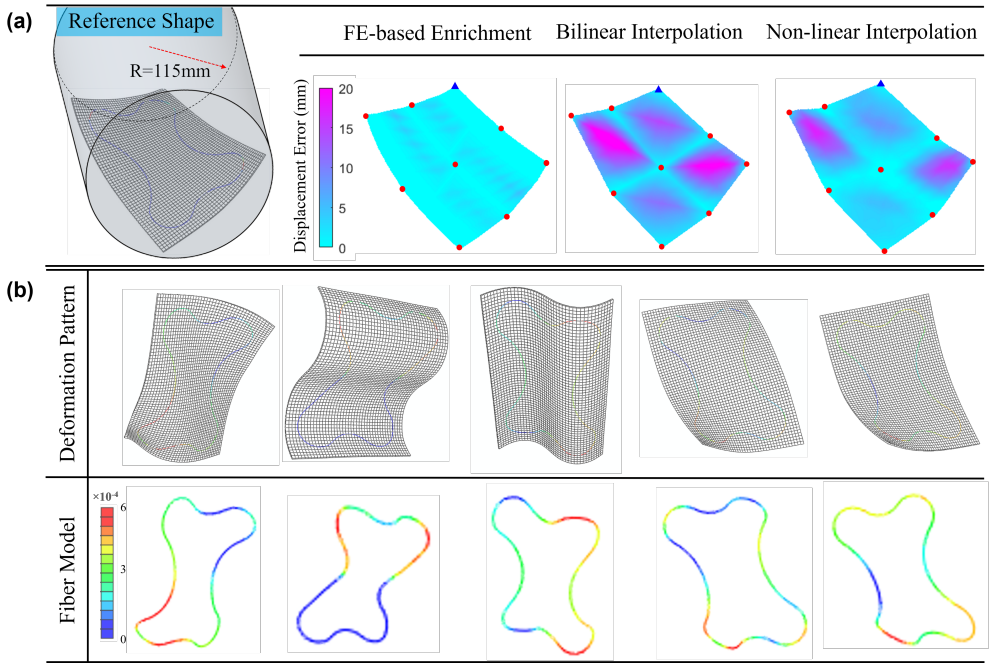

Figure 3.5. **(a)** Surface approximation based on nine query points over a cylinder of diameter 115 mm. Color bar showing the displacement errors for all three methods, namely FE-based enrichment, piecewise bilinear interpolation and triangle-based non-linear interpolation [80]. **(b)** Simulated deformation patterns and its fiber strains based on nine query points.

However, it may not be feasible as the number of query points influences the complexity of model training and hence its performance. It should be noted that the errors stemming from data enrichment (from EM-tracked nodes to denser nodes) are part of the final sensing error, which also includes the

modeling error. The mean data enrichment error for a 3000-frame sample was 0.6995 mm. Five deformation patterns were selected in Figure 3.5 with their corresponding simulate strains. The variance in fiber strains indicates that a unique mapping is possible to differentiate different deformation patterns. The coefficient of determination R^2 is >0.999, showing that the simulated dataset was consistent with the acquisition.

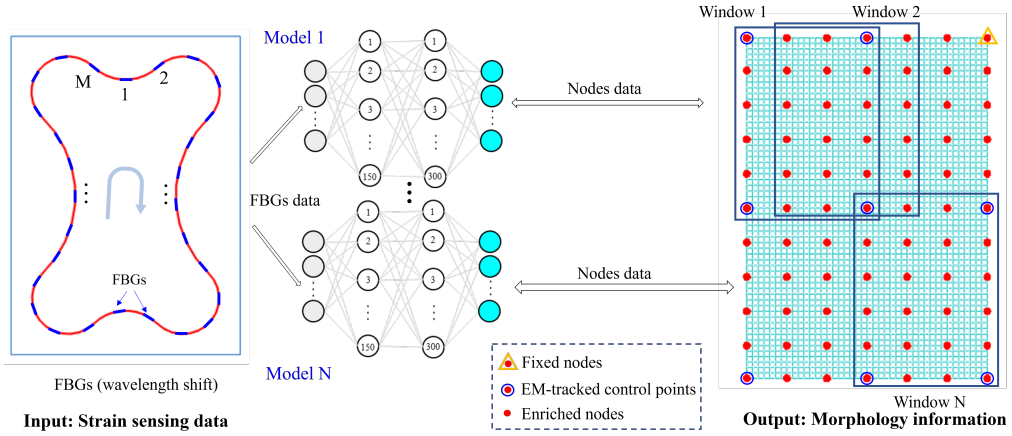

Figure 3.6. Proposed data-driven model using ensemble learning. The rectangular surface is divided into N windows of equivalent size and covering an equivalent amount of nodes. Each window corresponds to an multi-layer perceptron (MLP) regression sub-model. Altogether, twenty-eight (M) strain sensing data are used as inputs to twenty-four (N) two-layered MLP sub-models

3.3.2 Ensemble learning

Further from the FE-based data enrichment, an ensemble model was developed to map strains to a denser grid of enriched nodal displacements (Figure 3.6). Although the sensor shape could be realized by a denser grid, the issue of discrete point-wise sensing has become the primary source of errors. An ideal learning model should have regarded the deformation at the blank regions between FBG sensors, which could also be used for other grid-based sensor arrays. In this Chapter, the A4-sized prototype was divided into multiple smaller overlapping rectangular areas, where nodes within the same

area would be spatially related [81], [82]. The configuration took references from a technique called "sliding window" that is commonly used in image recognition classification problems [83], [84]. Within each region (window), the nodal displacements were modeled by an individual ANN-based sub-model. It implied that nodal displacements that were covered in overlapping windows would be calculated and cross-validated. The overall model prediction was ensembled by the weighted prediction of multiple sub-models [85], [86].

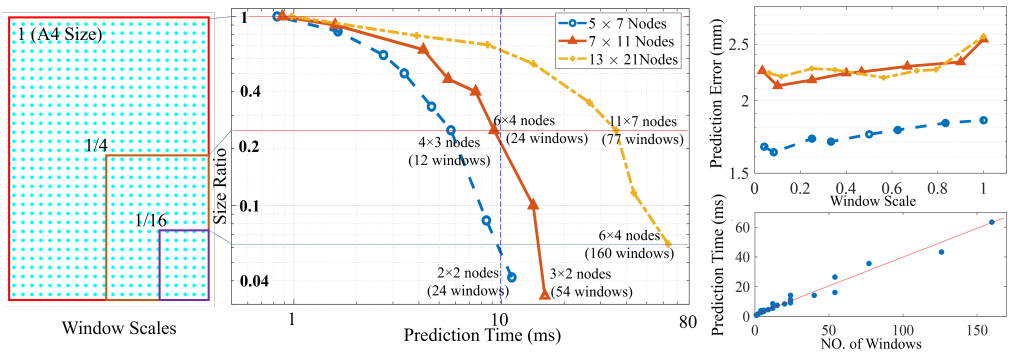

Figure 3.7. Analysis of the trade-off between prediction accuracy and computational time.

By controlling the number of nodal displacements (node density) and windows (sub-model size), the trade-off between prediction accuracy and computational time was analyzed. As summarized in Figure 3.7, small sub-model size and denser nodes resulted in higher accuracy and longer computational time. Out of the combination of three node densities and eight window sizes, the prediction time ranges from 1 ms to almost 80 ms. The time is much smaller than a full iteration of FEA that runs for hours or days. The prediction error fell in a narrower range between 1.5 to 2.5 mm. Whether such error size is sufficiently small to enable accurate shape sensing requires further experimental validation and characterization analysis. The above preliminary results show that it is possible to establish a data-driven modeling approach to realize large-scale shape sensing with low temporal latency. To experimentally

validate its feasibility, multiple tests were carried out with a configuration of 7 × 11 nodes and 24 windows. The corresponding computation time of 10 ms (100 Hz) was comparable to human proprioception which could be a benchmark for developing biomimicking robots and senses-enhancing wearbales [87]–[89].

3.4 Experimental evaluation of a A4-sized sensing skin

To evaluate the accuracy of data-driven modeling, the sensor prototype was subjected to a series of deformation patterns continuously. The shape reconstruction of three key instances is shown in Figure 3.8, all having a maximum nodal displacement of 60 mm.

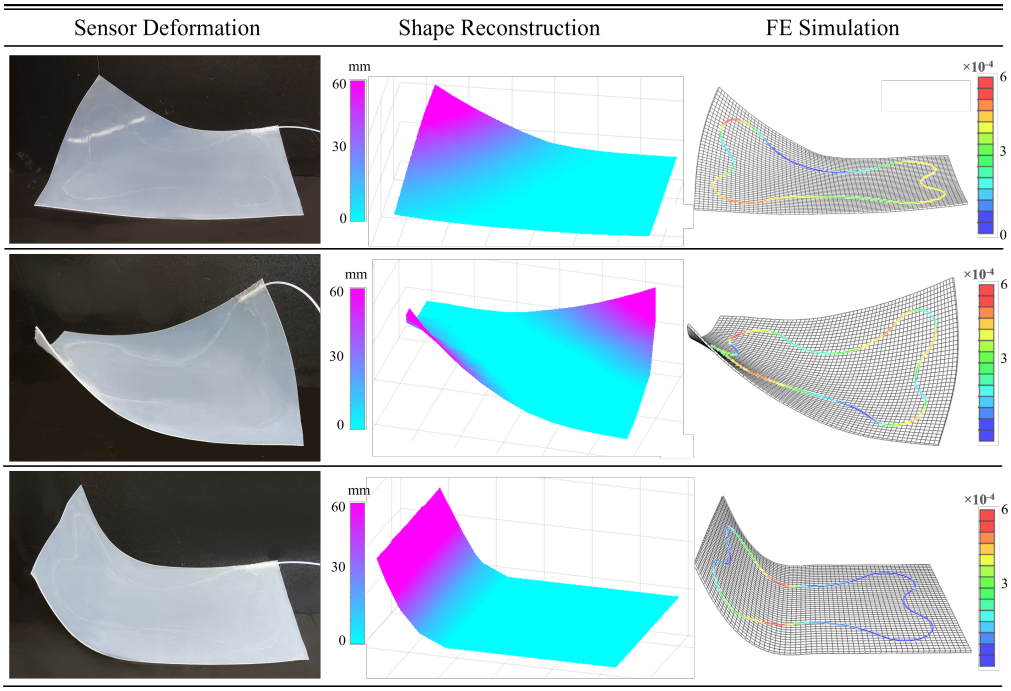

Figure 3.8. Selected shape reconstruction instances. The deformation pattern is reconstructed using the proposed data-driven model with color bar indicating the continuous displacement. The simulated fiber strain and enriched nodal displacements are also shown at the last column.

3.4.1 Model Prediction Accuracy

The deformation was compared with the EM-tracked ground truth nodes. Quantitatively, 300 deformation instances that had not appeared in the training dataset were analyzed in detail. The 2,700 nodal displacement errors (300 $\times$ 9 nodes) are plotted in Figure 3.9**(a)**, where 90% samples were smaller than 5 mm with RMSe 2.28 mm. Combined with the previous data enrichment error, the mean error was below 3 mm. Furthermore, the error distribution from the viewpoint of each node is shown in Figure 3.9**(b)** and Figure 3.9**(c)**, the RMS errors obviously were correlated with their RMS displacement, as well as their location on the sensor. Corner nodes A1, K1 and K7 have the largest error, probably due to additional DoFs than other nodes.

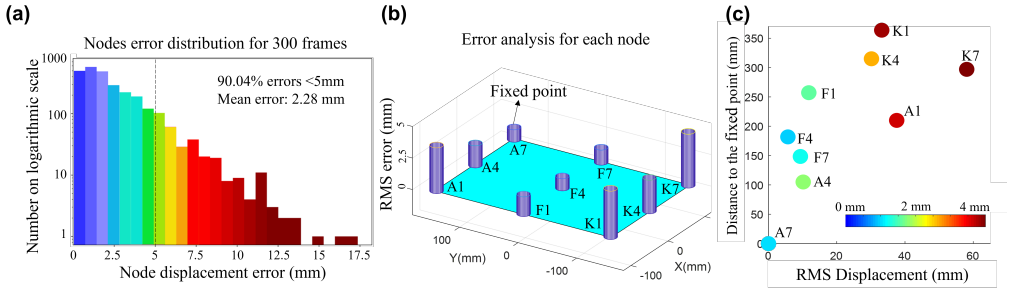

Figure 3.9. **(a)** Displacement error distribution of 2,700 samples selected from 300 frames (9 nodes). **(b)**RMS error of each EM-tracked node with A7 being the clamped point. **(c)** RMS error distribution in **(b)** against the distance from A7 and RMS displacement.

When further looking at their prediction errors during deformation over a period of 10s (Figure 3.10), the prediction of 3-D nodal displacements still follows a similar data shape for all instances with errors mostly below 5 mm, but could go up to 15 mm. Using a maximum nodal displacement of 60 mm, the 25% error was beyond the acceptable limit of shape sensing. In those instances, the shape reconstruction deviated from the actual deformation even for visual representation since nodal errors of neighboring regions were related by ensembled models. The 15 mm large error at K1 was implying an

error >10mm of its neighboring enriched nodes. The use of FEA and ensemble learning had regarded the soft sensor as a continuous body, eliminating the possibility of absurd prediction of one large error happening on only one node. It failed to eliminate/mitigate the deviations for all nodes that possibly derived from one single error. In those instances, the shape reconstruction might not have a noticeable issue. If used for any other application, such visual feedback might lead to wrong decision-making, and thus should be seriously regarded.

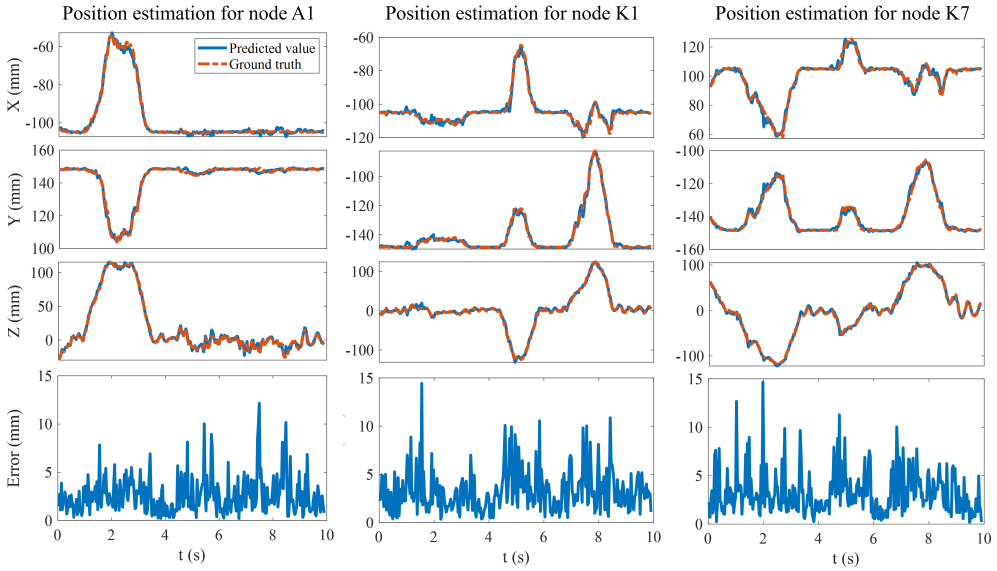

Figure 3.10. Positions estimation on nodes with larger error. During a period of 10 seconds of continuous deformation, the 3-D errors of nodes A1, K1 and K7 were computed. No special deviations in a particular dimension can be seen. The deviation mostly falls below 5mm with exceptions reaching 15 mm.

3.4.2 Hysteresis and Repeatability

In addition to accuracy, the sensor prototype was characterized by 1000 repeating cycles of one-end-clamped bending at 0.5 Hz in Figure 3.11 The sensor was bent upward, downward, then back to the neutral position, driven by a linear actuator at the distal edge. The raw Bragg wavelengths of three FBGs were also monitored for hysteresis analysis. Based on the relationship

between the wavelength shift λ_m and mechanical strains ϵ_m, the hysteresis for strain sensing is of equivalent order to the hysteresis of Bragg wavelengths.

$$\epsilon_m = \frac{1}{\mathrm{k}}\left(\frac{\lambda_m}{\lambda_{m0}} - \frac{\lambda_c}{\lambda_{c0}}\right) \tag{3.1}$$

where λ_{c0} and λ_c refer to the original wavelength and wavelength shift of compensation FBG respectively, λ_{m0} and λ_c refers to the original wavelength and wavelength shift of the FBG for mechanical strain, $k = 0.78$ being the gauge factor [73]. The equation can be reduced to a simpler form with coefficient k_0 assuming no temperature variation,

$$\epsilon_m = \mathrm{k}_0 \lambda_m \tag{3.2}$$

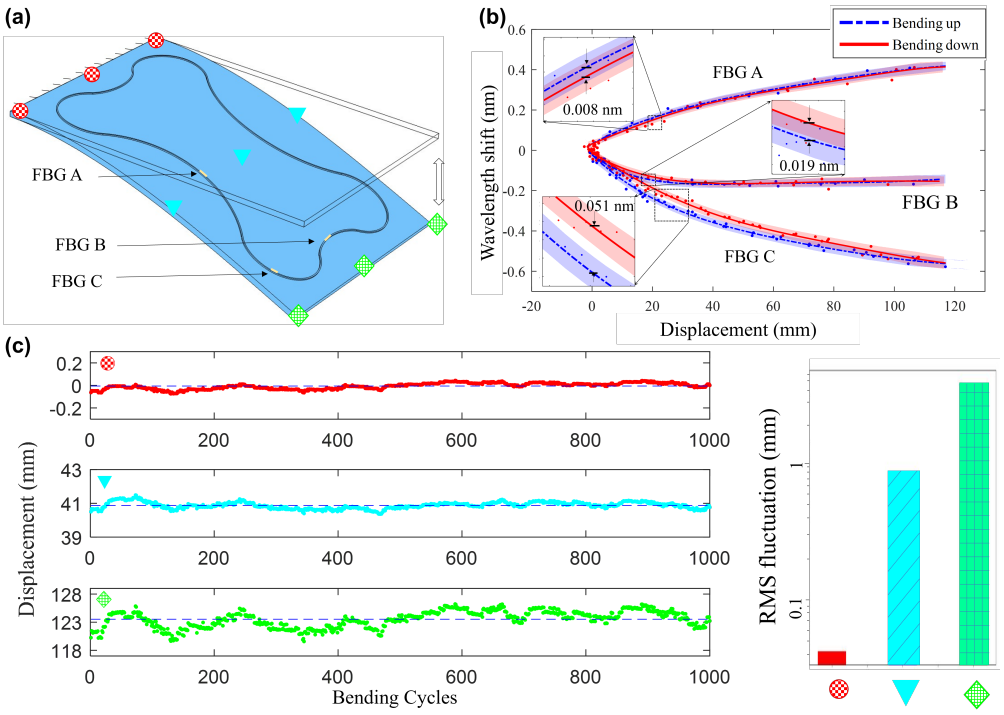

Figure 3.11. **(a)** Setup for hysteresis and repeatability tests. Three FBGs at different locations were selected. **(b)** Hysteresis plot of wavelength shifts against simple upward and downward bending. **(c)** Fluctuations of predicted displacement over 1000 repeating cycles at 0.5 Hz. **(d)** Logarithmic representation of fluctuations.

By plotting the fitting curve and 95% confidence interval (shaded region), the hysteresis between upward and downward bending was found. Depending on the FBGs location, the disparities vary with a maximum 0.051mm shift. The small value showcased that adhering FBGs on a soft medium had no influence on its strain sensing capability. For data-driven modeling approaches that utilize other sensors for raw signals input, the disparity should be highly regarded as it directly influences system robustness. The training model makes no sense if the raw inputs vary too much. For this sensor prototype, the fluctuations in prediction after 1000 cycles remain at a very low level with the largest RMS fluctuation of 1.48 mm as shown in Figure 3.11**(c)** and logarithmic scale in Figure 3.11**(d)**). The small fluctuations suggest that not only FBG strain sensing remains robust, but also the adhesion was durable such that the optical fiber conforms to the deformed shape in all bending cycles.

3.5 Large-scale shape reconstruction underwater

Following the workflow in previous sessions that develop a data-driven modeling approach for a large-scale rectangular shape sensor (Figure 3.1), a fish-shaped shape sensor was developed. The structure and its virtual model are shown in Figure 3.12, using equivalent silicone rubber and optical fiber. The primary goal was to validate whether the modeling approach and shape sensing is applicable underwater. Given a series of training data acquired up in the air, the shape sensor was tested in a water tank with external hydrodynamic force. The fixed part of the prototype was linked to a rod actuating axially at 1 Hz, where the silicone body was deformed by buoyancy force and ever-changing waves. In such an unfamiliar environment and with optical fiber directly exposed to water, the real-time shape reconstruction of the fish-shaped sensor is shown in Figure 3.12**(d)**. The results build up

confidence for this data-driven modeling approach to be used in underwater applications (e.g. marine robots [90], [91]), as well as biomimicking robots [92].

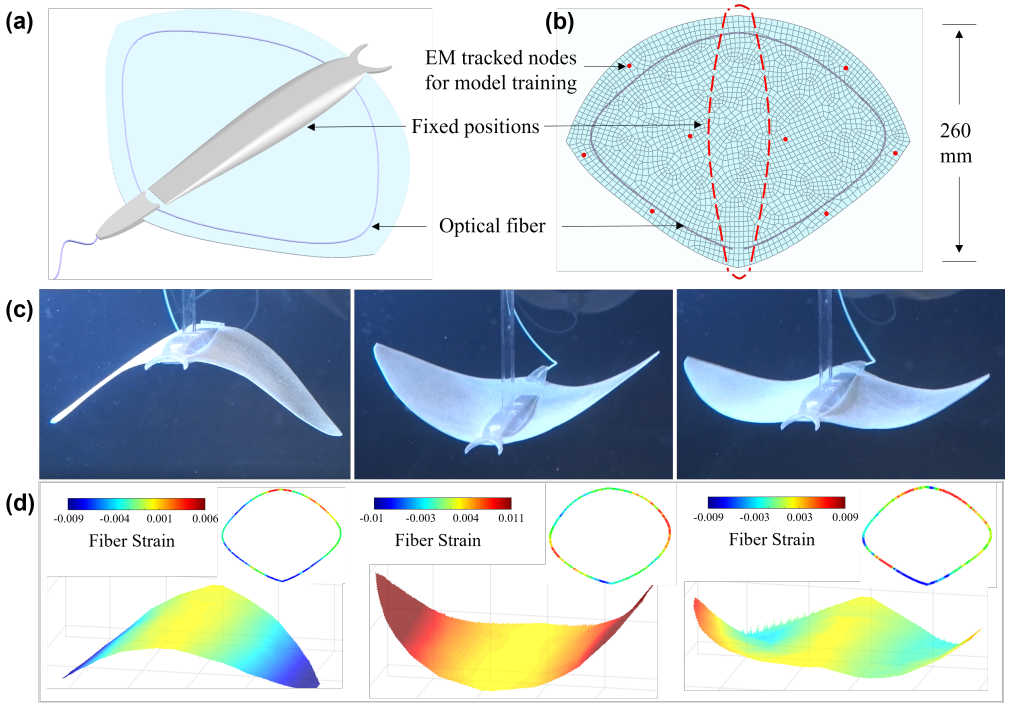

Figure 3.12. Shape sensing of the fish-shaped prototype underwater. **(a)** Sensor design using the workflow in Figure 3.11 (b) The FE mesh of the fish-shaped prototype. **(c)** Three instances during deformation. **(d)** Corresponding shape reconstruction in real-time. Color bars refer to fiber strains.

3.6 Conclusion

In this Chapter, a data-driven modeling approach for large-scale shape sensing is step-by-step developed. The motivation for incorporating each component/tool is discussed, with reference to the challenges mentioned in Chapter 2. In explicit, two sensor prototypes were developed with an FE-based design analysis before their fabrication. The overall sensor configuration was determined based on simulated strain responses, such that a dog-bone-like FBGs-carrying optical fiber routing over a 1mm thick substrate could capture strains all over the sensing area safely and durably. Utilizing the same

simulated environment and motion capture technology, sensor shape could be approximated by denser nodes with minimized errors compared with conventional interpolation techniques. The issue of high computational cost in iterative computational mechanics was eliminated by the introduction of a training model; While the difficulty in acquiring sufficient high-quality training data was overcome by the data enrichment in FEA. The trade-off between prediction accuracy and computational time was balanced by controlling the parameters in an ensemble learning configuration, where the shape sensor was divided into multiple sub-models with adjustable node density. The division successfully transformed the discrete nodes array into a continuous body, where deformation at every location is spatially related to its neighboring region. The combination of all these tools enables shape sensing over an A4-sized (210 $\times$ 297 mm) with an RMS error of 2.28 mm at 100 Hz. It was durable and functional after 1000 repeating cycles with a maximum fluctuation of 1.5 mm. Underwater demonstrations showcase additional potential to be used in other harsh environments where training data can be acquired elsewhere. In these scenarios, more requirements have to be fulfilled despite the demonstrated accuracy and repeatability.

Mobility/portability is one of the push factors for FBGs shape sensor as reviewed in Chapter 2. Imagine a marine robot designed to freely explore the sea, the tethered connection for interrogating wavelength shifts would be restrictive to its motion planning. Regardless of sensing capability, mobility in those scenarios is prioritized over many other functionalities. To push the data-driven modeling approach a step forward in task-based applications, untethered sensing alternatives over FBGs should be considered. Among all soft sensing options reviewed, optical waveguide sensors can be made portable since light transmission does not require a return path to an interfacing machine. However, there does not exist any convincing solutions to

realize high-order soft sensing with optical waveguide sensor. In the next Chapter, a optical waveguide sensing approach is proposed with a generalized learning-based framework based on the data-driven modeling approach.

Chapter 4

Self-Contained Shape Sensor Empowered by an Autoregressive Learning Framework

4.1 Introduction

The study of light transmission underpins the fundamental development of many optical devices and photonics technologies [5], [93]. In the area of geometrical optics, light transmission can be approximated as the propagation of rays [94], and has been utilized in waveguide-based sensing [63], [95]–[98]. Given a flexible medium of homogeneous refractive index with cladding, light rays are guided like a pathway resulting from total internal reflection. However, light transmission variations in light intensity and refraction losses can occur due to external mechanical stimuli. In Chapter 2, the reviewed application of waveguide sensors spans many fields and shows potential as an alternative to flexible electronics and optical fiber-based sensing. This is particularly true when the primary design goal of such "soft sensors" or

"electronic skins" is the reconstruction of the sensor's deformation or morphology in multiple dimensions, often requiring high flexibility and some degree of stretchability. In the prior art, LED and PD pairs are typically placed at either end of a thin waveguide, providing 1D measurement per waveguide. Transmission loss takes advantage of geometrical optics, reducing formulation and modeling complexity often found in the light modulation approach [99], [100]. Generally, simplified PD-LED-based sensors serve as an interesting proposition with low fabrication costs, ease of scaling, and potential for unique waveguide and component placement.

Regardless of the sensing approach, combining multiple low-level sensors to predict high-order morphology changes remains challenging, particularly for soft mediums, which possess infinitely possible degrees of freedom [101], [102]. The substantial complexity in computing finite sensory information for high-level state estimation requires novel hardware design and modeling methods. Chapter 3 proposes a data-driven modeling approach with the help of computational mechanics and simple AI models. Simulated data tremendously reduces the density of transducing units while providing infinite possible virtual strains and displacements. This data enrichment method can provide significant benefits in cases where limited ground truth data are available to estimate a complex surface. When supplied with a comprehensive and consistent set of simulation outputs, data-driven mapping between sensory data (e.g., resistance/refracted wavelength) and mechanical stimuli (e.g., pressure/shape change) can be modeled. With data-driven modeling, convincing performance is shown in both classification (e.g., the spatial accuracy of pressure) and regression tasks (e.g., pressure magnitude estimation) [103]. However, a specialized neural network architecture for high-order sensing outputs requires much more research to explore and verify.

In Chapter 3, several multilayer perceptrons (MLP) models were

ensembled to predict the displacement of markers on a flat silicone sensor with strain measurements given by FBGs. However, it was occasionally observed that the prediction could momentarily deviate from the ground truth significantly, which may be caused by overlooking the data's temporal characteristics. Recurrent neural networks (RNN), such as long short-term memory (LSTM), are also popular in soft sensing [104]. An example of a single-layer LSTM combined with an MLP was used to predict the magnitude of contact force with an average error of 0.05±0.06 N in a soft finger [105]. However, a notable delay was present, possibly caused by the high computational cost of LSTM. Convolutional neural networks (CNN) are utilized in sparsely distributed sensors, e.g., a CNN layer was used to classify stimuli type exerted on robotic skin with an accuracy of 98.7% [106]. However, the criteria for selecting such learning-based methods were not explained in previous research, and thus it is challenging to determine the appropriate framework for newly developed soft sensors.

In this chapter, a general framework for flexible surface shape sensing in real-time is presented on a soft and self-contained optical waveguide sensor using sparsely placed PD and LEDs. It takes advantage of finite element (FE) modeling to assist sensor parameter design, as well as sparse data enrichment in Chapter 3. Additional multi-physics simulation that optimizes training data spatiotemporal characteristics is covered prior to the detailed investigation of an autoregressive-based learning model.

4.2 Proof-of-concept optical waveguide sensing

An A5-sized soft skin (148 × 210 × 4 mm) embedded with three pairs of LED and PD was developed to demonstrate the working principle of the raised waveguide sensor. Before the fabrication of the real prototype, the light transmission inside the skin was simulated using FE to investigate the

influence of PD-LED's distribution on the light signal. And thus, suggestions on the location of sensing elements were proposed. The distribution of sensing elements (i.e., LED and PD) in the proposed shape decoder is discrete and their locations would affect the light intensity data. To create the light-deformation mapping using a data-driven method, the data pair is required to be one-to-one, i.e., one kind of skin state corresponds to only one set of light intensity, and vice versa. Additionally, the data dimension must be sufficient to support the recognition of high-order skin deformations. To satisfy such requirements on data quality, the optimization of LED and PD locations is expected. Before optimization, an FE model was established to investigate the influence of sensing unit distribution on light intensity.

4.2.1 Simulation settings

The A5-sized waveguide sensor was meshed into 1260 C3D8IH elements with equivalent material properties in the simulation software COMSOL Multiphysics, where geometrical optics and solid mechanics modules were utilized. The refractive index of PDMS is varied with light wavelength, the lower wavelength with the higher refractive index, such that Red (700 nm) with 1.4273, Green (510 nm) with 1.4364 and Blue (440 nm) with 1.4433 [107]. Light rays in these three colors, each simulated with 5,000 vectors, were emitted based on a Lambertian distribution. The simulated light loss was set at a reflection coefficient of 0.75. Zero polarization is assumed. A stationery study with nonlinear geometricity was carried out for deformation at step 1 (t = 0), followed by a ray tracing study at step 2 (t = 20 ns).

4.2.2 Simulated results analysis

In the first simulation, three LEDs and a PD were respectively placed at the clamped and free end of an A5-sized rectangular waveguide, which would be

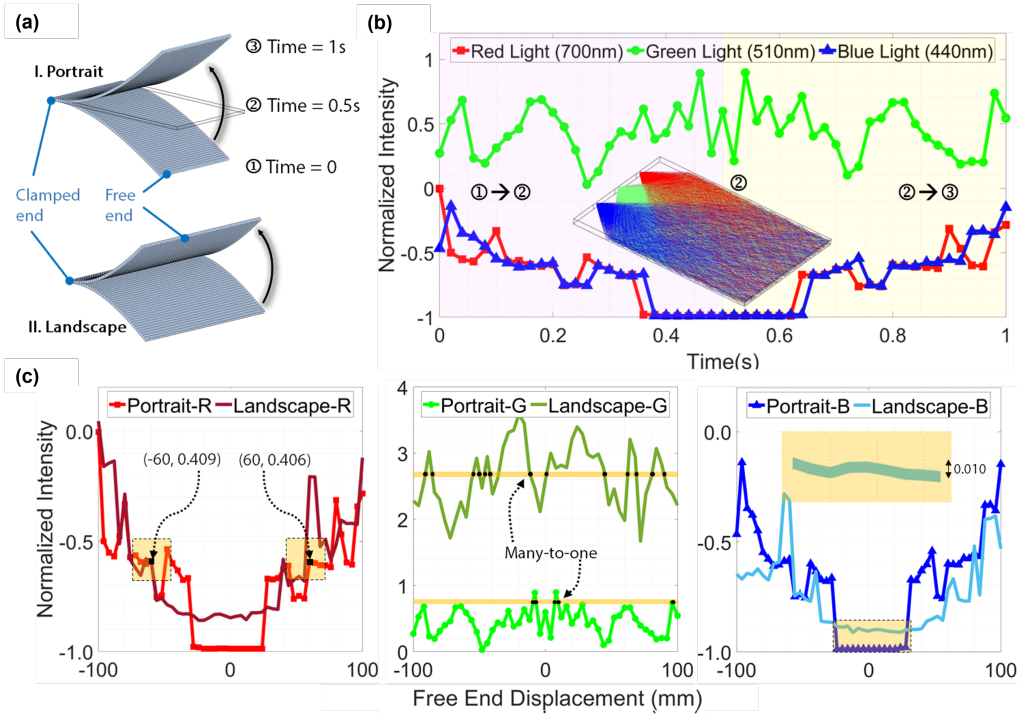

Figure 4.1. FE geometrical optics analysis of an A5-sized waveguide without design optimization. **(a)** Simple bending with one end clamped along two orientations (i.e., portrait and landscape orientation). **(b)** Simulation normalized light intensities at the free end during portrait flipping motion, supplementing the schematic of RGB light transmission inside the skin at the flat state (time=0.5 s). **(c)** Problems in RGB light intensities along with the free end displacement for both flipping modes (highlighted)

deformed in two modes, i.e., portrait and landscape as shown in Figure 4.1**(a)**. The light from LEDs would experience reflection and refraction before being captured by PD, which would lead to light intensity loss. As shown in Figure 4.1**(b)**, light signal responses are almost symmetric for all three wavelengths during the downward (① ∼ ②) and upward (② ∼ ③) bending, namely, the light signal captured under different skin deformation is the same, which is a hinder to motion modeling. The same problem would appear in the landscape mode where the free-hanging length is shorter. During small displacement (free end displacement < ±20 mm, the Red and Blue light intensities are nearly zero as the Red and Blue lights were put close to the side wall and most of the light rays were absorbed or refracted. Besides, the spiky noise is obvious. In sum,

the problems of symmetricity, zero light intensity variation and noise would appear when the arrangement of LED and PD pairs is not optimized. Since the low-quality data is highly unfavorable to sensing resolution as well as data-driven modeling, therefore the angle α and distance D between LEDs and PD as illustrated in Figure 4.2 should be optimized, which are dominant factors to the captured light intensity.

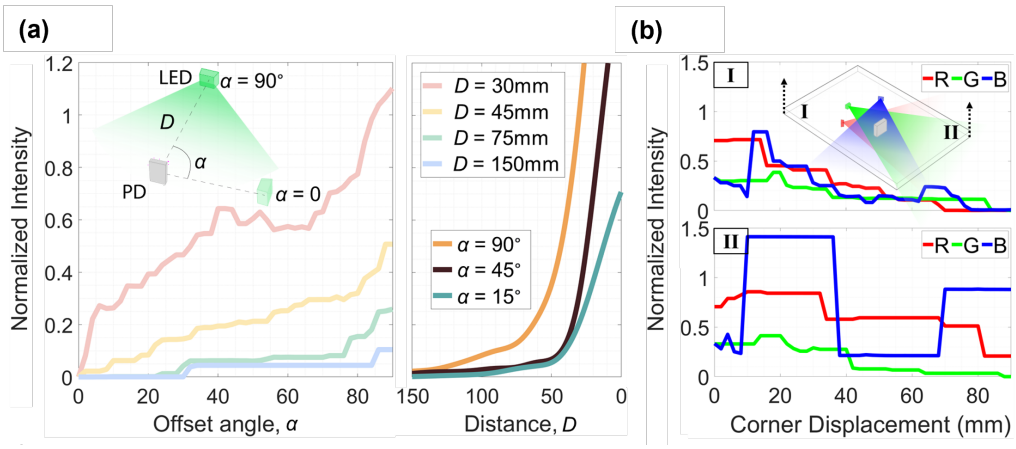

Figure 4.2. Design optimization of LED and PD placement, and validation in an A5-sized sensor (148 × 210 × 4 mm). **(a)** Simulated light intensity variations in terms of absolute distance D and the offset angle α between the LED and PD. **(b)** Simulated light intensities when bending two opposite corners (I and II) of the skin embedded with three LEDs (Red, Green, and Blue) and a PD.

The light intensities measured at 46 angles α ranging from 0 to 90° and four distances D ranging from 30 to 150 mm were compared in Figure 4.2**(a)**. For a specified angle, the light intensity drops exponentially with the distance. Most primary rays would undergo free scattering and cannot focus on PD through a specific pathway like conventionally in optical fiber, and hence extended distance would bring increased light loss. Under a fixed distance, the angle of 90° is optimal as the PD can only receive light from the front side. As displayed in Figure 4.2**(b)**, the light transmission inside a skin sensor with the optimized setting is simulated, where the angle α and distance D from the PD to Red, Green and Blue LEDs are respectively 45, 90, 150°, and 45, 60, 60 mm. When bending the skin sensor upwards by the top left corners as shown in

Figure 4.2**(b)**I, the light intensity is varying continuously without plateau phases, and thus one type of shape corresponds to one set of light. However, as shown in Figure 4.2**(b)**II, the zero light intensity variation, i.e., plateau phase, still exists in all colors. This implies the need for optimizing PDs/LEDs allocation and distribution, or the numbers of LED-PD pairs to increase the data dimension.

4.2.3 Experimental validation

To demonstrate the optimized sensing effect, a 5-layered PDMS silicone sensor (148 × 210 × 4 mm) with three pairs of LED and PD was fabricated, the distribution of which were following the simulation. Explicitly, PDs were placed near the edge of three sides, facing to the center of the rectangular sensor; RGB LEDs were placed at the range of 45 mm< D < 60 mm and 30°< α <150°, facing towards the nearest PDs.

The sensor is composed of three main parts, namely the soft skin, sensing elements and wireless data transmission modules. The soft skin works as the medium of light transmission, consisting of five layers as shown in Figure 4.3**(a)**. Isotropic and non-dispersive PDMS is commonly used as the substance for light-transmitting due to its high refractive index (≈1.4) and transmittance (>90%) for visible light [107]. The fabrication of soft skin followed the standard silicone curing process (Figure 4.3**(b)**, which was repeatedly carried out for all layers. The mixed PDMS (Sylgard 184) in a 10:1 ratio was degassed in a vacuum and cured under 60°C for 48 hours, followed by 120°C for 30 minutes. For the opaque and semi-opaque layers, PDMS was additionally mixed with silicone dye. RGB LEDs (Kingbright 0603 LED), PDs (AMS TCS34725FN, 400 kHz) were respectively selected as light-emitting and transducing elements, both of which were embedded in the transparent layer. The electronics were connected to a Field Programmable Gate Arrays (FPGA) based printed circuit

board (PCB) with Bluetooth 5.0 (HC Tech, nRF52832) module and lithium-ion battery (3.7V, 400 mAh) as shown in Figure 4.3**(c)**. The battery life is approximately 30 minutes for consecutive sensing. These components are all off-shelf available in the market and interchangeable, for instance, the waveguide medium can be substituted by the synthetic hydrogel. The total estimated cost is 150 USD.

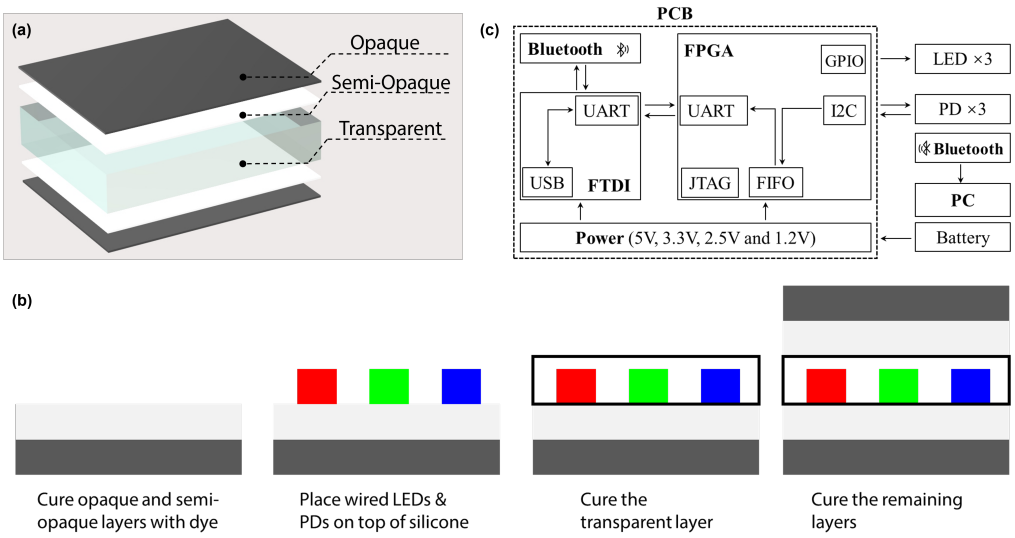

Figure 4.3. (a) Sandwiched PDMS structure of the soft waveguide sensor, where opaque and semi-opaque layers are silicone-dyed to enable internal reflection. **(b)** Schematic of the FPGA PCB used for both shape sensor prototypes. **(c)** Key fabrication steps of the sandwiched PDMS structure.

It can be observed that the light intensity is correlated with the bending type. For instance, when the sensor was lifted at its top left corner (1st column in Figure 4.4), the 1st (left) PD's signal varied obviously while the 3rd (right) one tended to be stagnant. This bending mostly affected the light transmission in the left and middle regions, while only having a slight effect on the right region's light path. When the sensor was lifted at the other three corners (other columns in Figure 4.4), the signal and motion are also consistent. With this optimized LED-PD setting, the discrete deformation pattern can be roughly observed corresponding to the plotting of light intensity data. For continuous

shape reconstruction in detail, a model capable of mapping light intensity to sensor shape is therefore explored. The soft skin shape reconstruction through analytical light transmission modeling needs large computational time and assumptions, which conflicts with the requirement of high-frequency response and high-accuracy sensing on sensors in practical use. Therefore, by exploiting deep learning to create the end-to-end mapping between light signals, skin configuration could be represented by 3-D coordinates of those evenly distributed nodes.

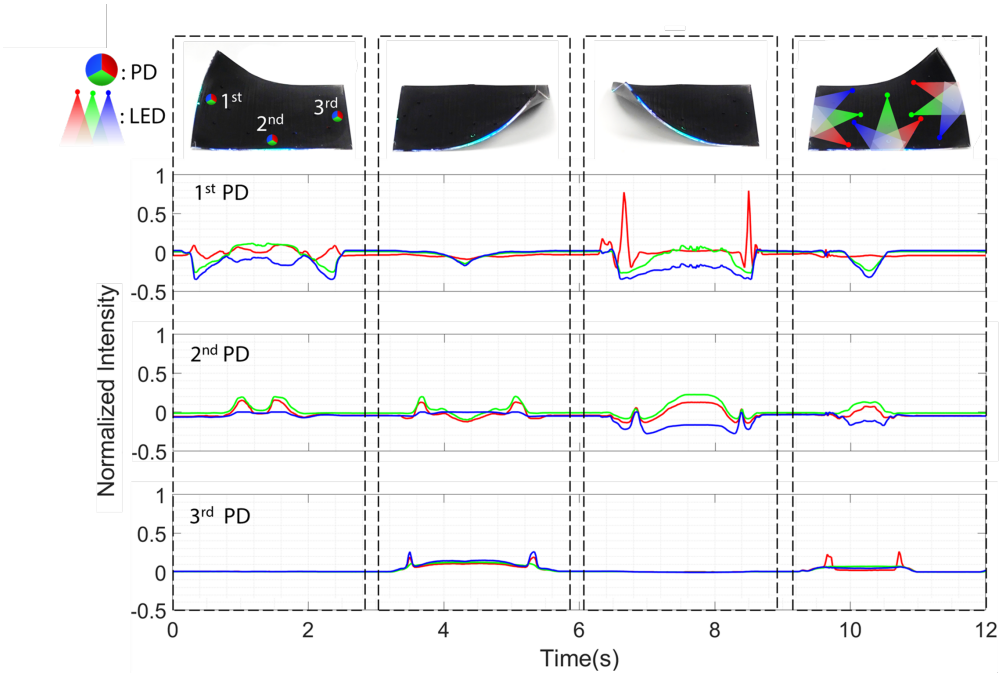

Figure 4.4. Optical waveguide design optimization validation. Three pairs of LED and PD were embedded in a A5-sized waveguide sensor and validated on multiple deformation patterns (1st row). Light intensity variations of each pair are shown respectively in the 2nd to 4th rows.

Prior to the training attempt using various models, an analysis of sensing data was carried out to observe the spatial and temporal characteristics, as well as to select appropriate learning models. Considering the skin deformation is of spatial locality, the points on the skin surface are grouped referring to their location as shown in Figure 4.5**(a)**, and inspected the average

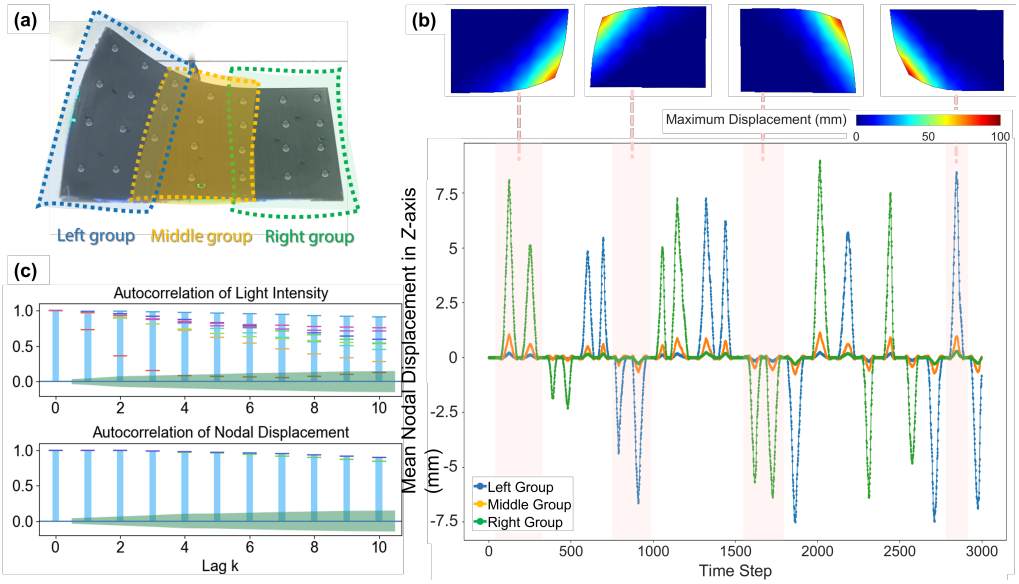

Figure 4.5. Data analysis on the light intensity and nodal displacements. **(a)** Nodes on the skin surface are clustered into left, middle and right groups. **(b)** Average z-axis nodal displacement of the three groups and corresponding skin deformation patterns during a series of bending motions. **(c)** Autocorrelation function (ACF) of light intensity and grouped node displacement with lags ranging from 0 to 10. The blue bar represents the maximum value in all channels under a specified lag, short colored horizontal lines are ACF of data channels (i.e., nine light intensity channels and three node displacement channels), and the green shaded regions are corresponding error bands.

z-axis displacements of these three groups during the bending deformation. The node coordinates have an obvious tendency along with the skin bending, i.e. when the top/bottom right (left) corner was deformed, the coordinates of the node in right (left) group would vary sharply; and the coordinate variation of nodes in middle group is relatively mild since the corner bending has a few effects on them. It can be referred to that the data is of spatial locality, and therefore, some techniques targeting spatial data such as convolution operators and patch-wise processing can be considered in the model. Since the bending is a continuous rather than impulsive motion, it can be supposed that the data is also very time-sequential, which means the historical signal would hold influence over a period of time further. To determine whether the model for time series is suitable for the study, we used k-order ACF to analyze the

light signal and node displacement:

$$\mathrm{ACF}(k) = \sum_{t=k+1}^{m} \frac{(y_t - \overline{y})(y_{t-k} - \overline{y})}{\sum_{t=1}^{n}(y_t - \overline{y})^2} \tag{4.1}$$

where $k = 1, 2, 3, \ldots$ is the lag value, y_i is the data at the i-th time step, $\overline{y}$ is the average value and m is the last time step. The ACF of light signal and node coordinates was evaluated using lag k ranging from 0 to 10, which could describe the degree of similarity between a time series and its lagged version [108]. As displayed in Figure 4.5**(c)**, most of the autocorrelation values exceed the error band and it can be deduced that the data has a significant autocorrelation. For such a time series, exploiting an autoregressive (AR) model to extract the time-sequential feature of data could be a feasible option, and evaluate complex motions such as the combination of bending and twisting.

4.3 Real-time intelligent shape sensing framework

To further evaluate the feasibility of the proposed shape sensing framework and the capability of the optical waveguide sensor, a fish-shaped prototype was designed. It was fabricated with reference to the previous rectangular sensor, following the same 5-layer sandwiching structure and electrical connection to FPGA board shown in Figure 4.6**(a)**. High frequency validation was performed underwater of hydrodynamic forces to evaluate the robustness of the AR-based shape-decoding accuracy.

4.3.1 Training Data Preparation

The volume and quality of training data vitally influence the training model and the sensing capability regardless of application and scenario. In Chapter 3, the combined use of motion capture technology with FE-based enrichment

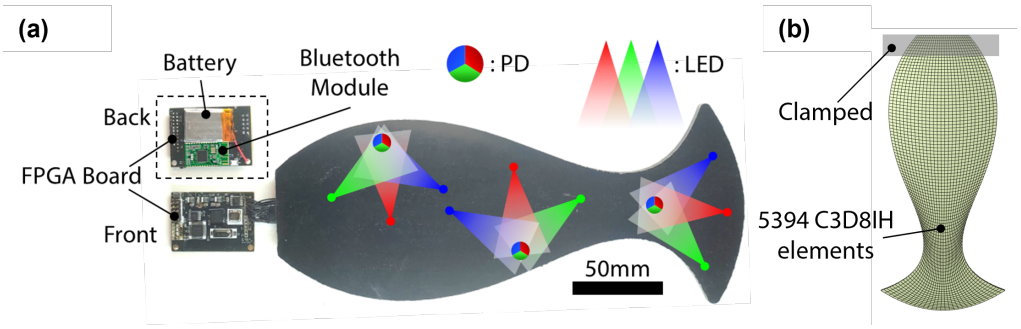

Figure 4.6. (a) Components of the fish-shaped waveguide sensor. Three pairs of PD and LED were embedded and connected to an FPGA board that carried the Bluetooth module and battery for data transmission. **(b)** Mesh configuration of the FE simulation for data enrichment.

method provided substantial amount of noise-free kinematics dataset, which serves as a good reference for this fish-shaped sensor. Prior to model training, these enriched node coordinates were analyzed by ACFs.

To assess the sensor's shape-decoding performance, a total of 3,000 frames of data (2,300 for training and 700 for testing) were collected underwater. Each frame of data consists of light intensity (input) provided by PDs and 3-D nodal displacements (output). One end of the fish prototype was clamped inside the water tank and the rest body complied with the water flow. During deformation, light intensities were acquired by multiple PDs and transmitted by an FPGA board. Five EM tracking markers were sparsely adhered to the sensor to capture real-time 3D coordinates at 20 Hz (Aurora V3, NDI) similar to that in Chapter 3. Other motion-tracking methods (e.g., infrared-based or dynamic Lidar detection) could also be alternatives if the difficulty of line-of-sight is overcome. Light intensities are wirelessly transmitted to the processing PC (i9-12900H, RTX 3060, 16GB RAM) at 150Hz for shape decoding (also use for subsequent model evaluation and repeatability test). The FE model was fed with 3D coordinates of five markers as point displacement constraints, and generated 48 nodes' coordinates via the commercial software ABAQUS. Assuming the embedded optoelectronic components would not

affect the skin's flexibility, the waveguide medium PDMS was set as an elastic material with the Poisson's ratio of 0.495 [109], density of 965 kg/m3 and elastic modulus of 2.5 MPa [110]. The FE model was discretized into 5394 linear hexahedral elements with incompatible modes (C3D8IH), which deliver much better accuracy than the standard hexahedral element under bending deformation in Figure 4.6**(b)**

4.3.2 Model Architecture

When constructing the deep learning model to map the light signal to skin shape, it is required to consider two criteria: data characteristics and computation efficiency. Due to the skin motion's time-continuity and space-locality, the sensing data is time-series as well as spatial. Having considered the requirement for high update frequency in a real-time sensing application, a trade-off between the computational cost and accuracy of the proposed modeling was determined. Taking the aforementioned two criteria into account, models like LSTM and CNN may not be well capable of dealing with temporal signal data input and hence an autoregressive model was developed.

As shown in Figure 4.7, the input was divided into two modules, which represented light intensity at the current time-step t and nodal displacement at the last time-step t-1, respectively. The output was the nodal displacement corresponding to the current time-step t. The model can recursively generate and receive the nodal displacement, respectively, with the aim of data training and forecasting in tests. To enhance the continuity of prediction, a time window was defined for temporal data sampling, implying that both the input and output would be a series of frames within the fixed time range. To handle the spatial deformation variation, the nodal displacements have to be grouped into several clusters referring to their node locations. Mappings of each group

from the light signal to nodal coordinates would be processed using independent MLPs.

4.3.3 Underwater performance evaluation

Based on the above AR model, the enriched 48 nodal displacements were divided into 3 groups as shown in Figure 4.7**(a)** The neural networks with a batch size of 128 were trained using L2 loss:

$$\text{Loss} = \frac{1}{n}\sum_{i=1}^{n}\left|\left|x_i - x_i^*\right|\right|_2 \tag{4.2}$$

where x_i and x_i^* are respectively predicted and label nodal displacement, and n is the number of nodes. The data was sampled using a time window size of five frames (≈0.03 s).

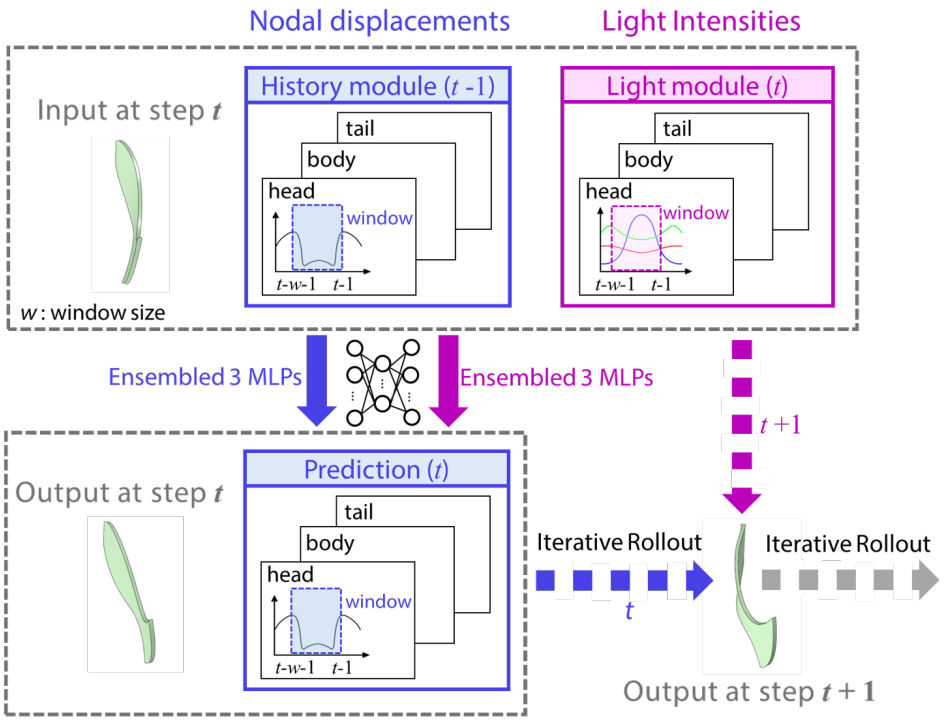

Figure 4.7. Model architecture of the proposed AR model. The model input consists of two parts, i.e., the history module storing the nodal displacement at the last step t-1, and the light module storing the light signal at the current step$t$. The output is the prediction of nodal displacement at the current step$t$. All the input and output are values during a period, namely the time window from t-w to$t$. The whole architecture is ensembled by 3 models, i.e., the head, body and tail models. The prediction rollout iteratively to the next step t+1 with nodal displacement at step$t$and light signal at step t+1, and so forth.

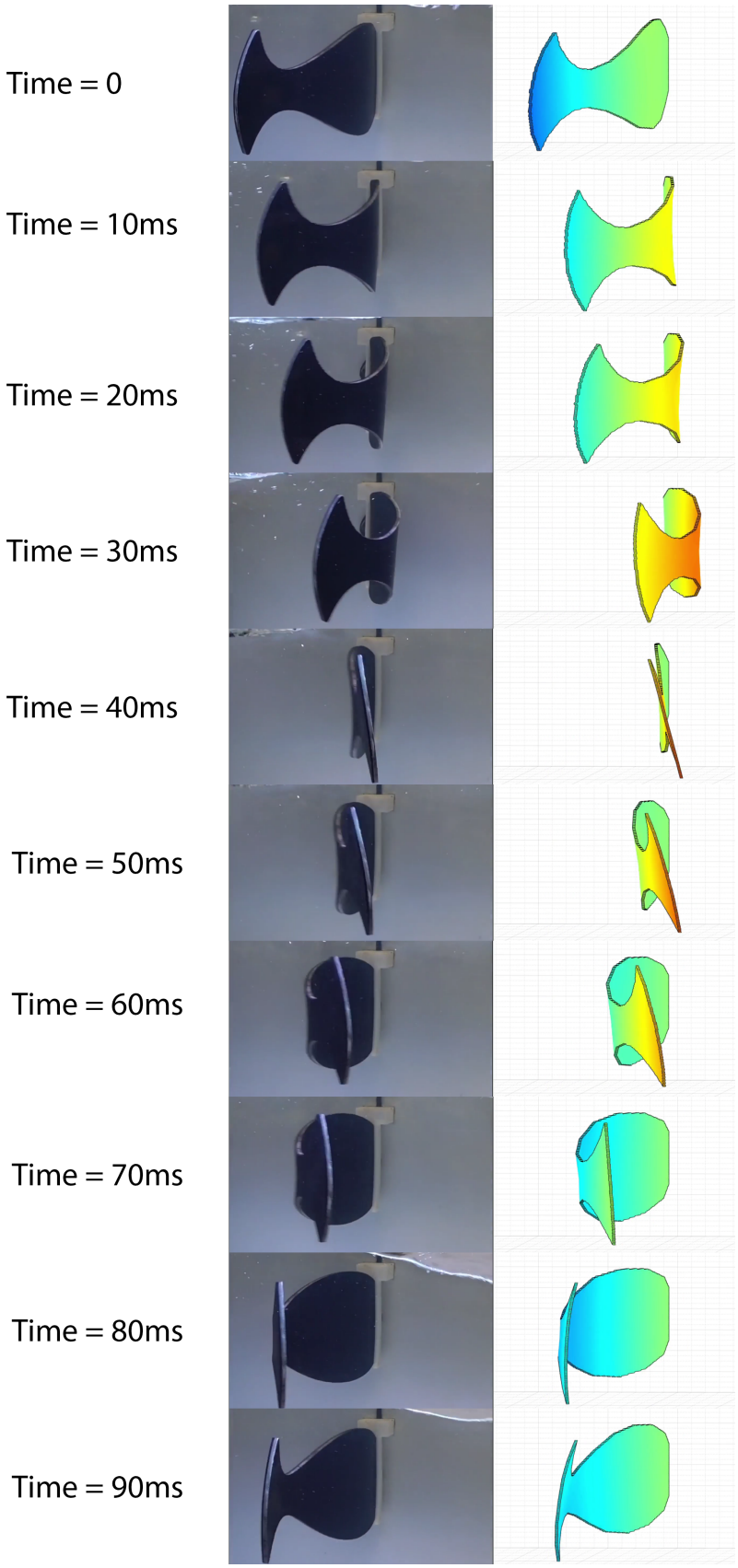

Figure 4.8. Real-time shape decoding (right) of the fish-shaped prototype underwater. Asymmetric deformation in response to the hydrodynamic force was captured at a 150 Hz sampling rate.

To enhance the generalizability of the model, both the input and output were values relative to the one in the stable initial state, and then normalized to zero mean and unit variance. All six MLPs in our architecture have four hidden layers with 128 neurons, taking ReLU as an activation function. Dropout (p = 0.5) was adopted to alleviate overfitting. To evaluate the performance of AR model, the fish-shaped sensor was placed in a water tank with one end clamped. The shape decoding performance can be previewed in Figure 4.8, visually showing that the model seems to be valid and accurate.

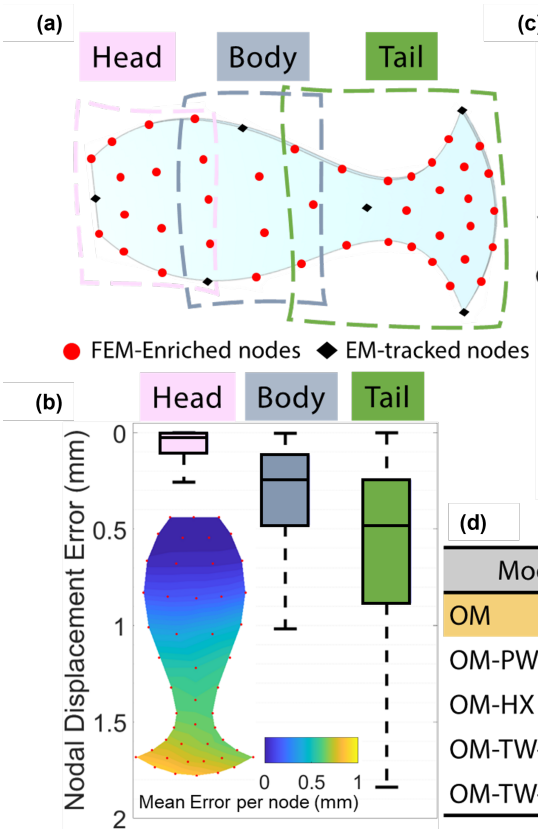

(d)

Models	RMSE (mm)	Median Error (mm)
OM	0.27	0.47
OM-PW	1.24	0.95
OM-HX	2.66	1.76
OM-TW-HX	2.67	1.99
OM-TW-HX-PW	3.75	2.62

Figure 4.9. Sensor shape and prediction performance through 33600 node instance samples collected from 700 frames. **(a)** Selected 48 nodes to represent the overall sensor morphology. **(b)** Distribution of nodal displacement error per group is illustrated in the box plot. **(c)** Distribution of nodal displacement error of all node instances. **(d)** Error comparison in the ablation study of removing time-window (TW), history (HX) module and patch-wise (PW) processing from the original model (OM).

For further analysis, errors are quantitatively investigated and discussed with an additional ablation study. The nodal displacement error distribution of three groups and 48 nodes are depicted in Figure 4.9**(b)** respectively and collectively in Figure 4.9**(c)**. It can be inferred that error would grow while the sensors are undergoing larger deformation, giving rise to the RMSEs of head, body and tail groups. An ablation study was conducted by removing three key components, i.e., time-window (TW), history (HX) module and patch-wise (PW) processing from the original model (OM) individually or jointly with an error comparison table shown in Figure 4.9**(d)** and histograms in Figure 4.10. In this ablation study, RMSE represents the mean error on 48 nodes in 700 frames, which is defined as

$$\text{RMSE} = \sqrt{\frac{1}{n}\sum_{i=1}^{n}\left|\left|x_i - x_i^*\right|\right|_2} \tag{4.3}$$

The smallest error among these five models indicates the importance of these components in terms of accurate prediction. As proved in the previous section, sensing data is a type of time series, such that the history module and time window data offering information on previous steps could play important roles. From the comparison between OM and OM w/ PW, we can conclude that patch-wise processing improves the model's ability to target the spatial locality of data.

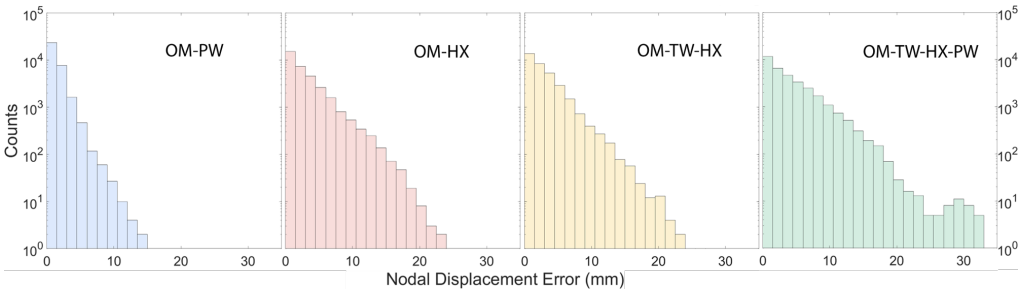

Figure 4.10. Extended histogram of nodal displacement errors in the ablation study.

With the comparison displayed in Figure 4.8 and Figure 4.11, the reconstruction is proved to be close to the ground truths, despite relatively

complex deformation, such as combining bending and torsion and inducing large (100-mm) displacement of the tail region. As displayed in Figure 4.11**(b)**, the shape reconstruction error is less than 5 mm during a 2-s deformation span without momentary large deviations, indicating that the decoding model could predict stably.

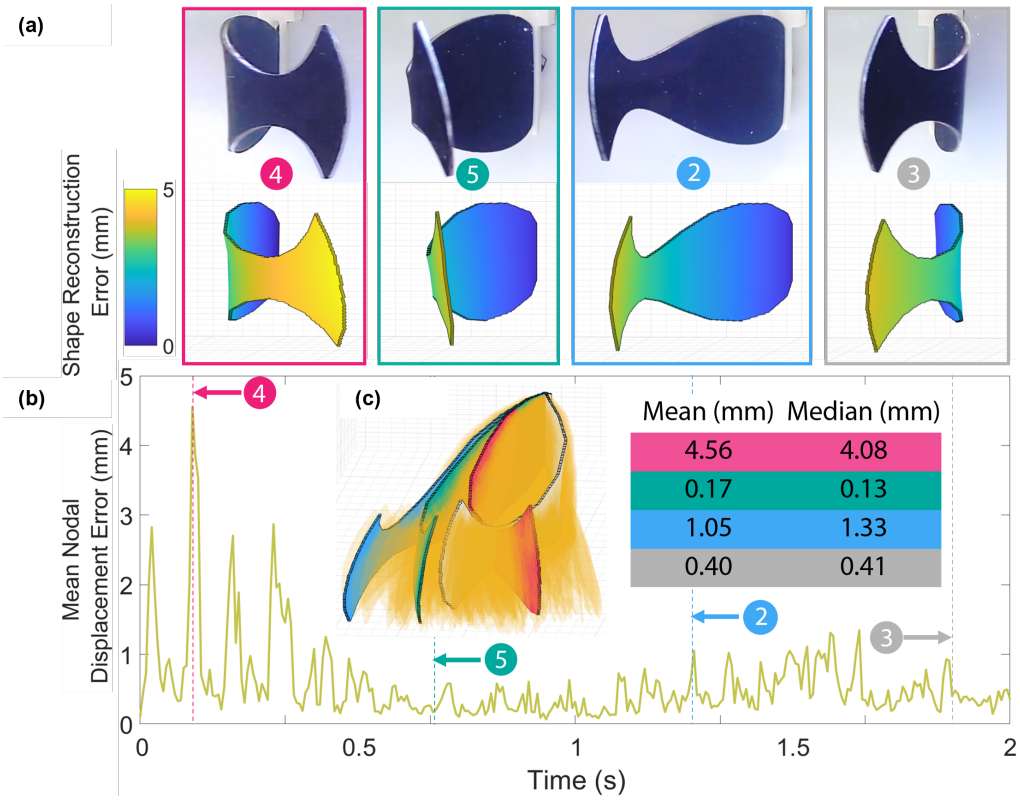

Figure 4.11. Shape decoding of the fish-shaped waveguide sensor in the underwater test. **(a)** Four different motion poses ② ③ ④ ⑤, and their corresponding decoded shape with colorbar showing the nodal displacement error. **(b)** Prediction error of decoded shapes during this 2-second deformation. The time of four motions in **(a)** was marked. **(c)** The isometric view of the reconstructed skin shape. The colored shape referred to the four poses in **(a)** and all predicted shapes (orange) within the 2s motion.

To further verify that the proposed waveguide sensing method is sufficiently robust for potential task-based application, a repeatability test of 1000 deformation cycles was conducted. The fish-shaped prototype were repeatedly undulated in the water driven by external hydrodynamic force

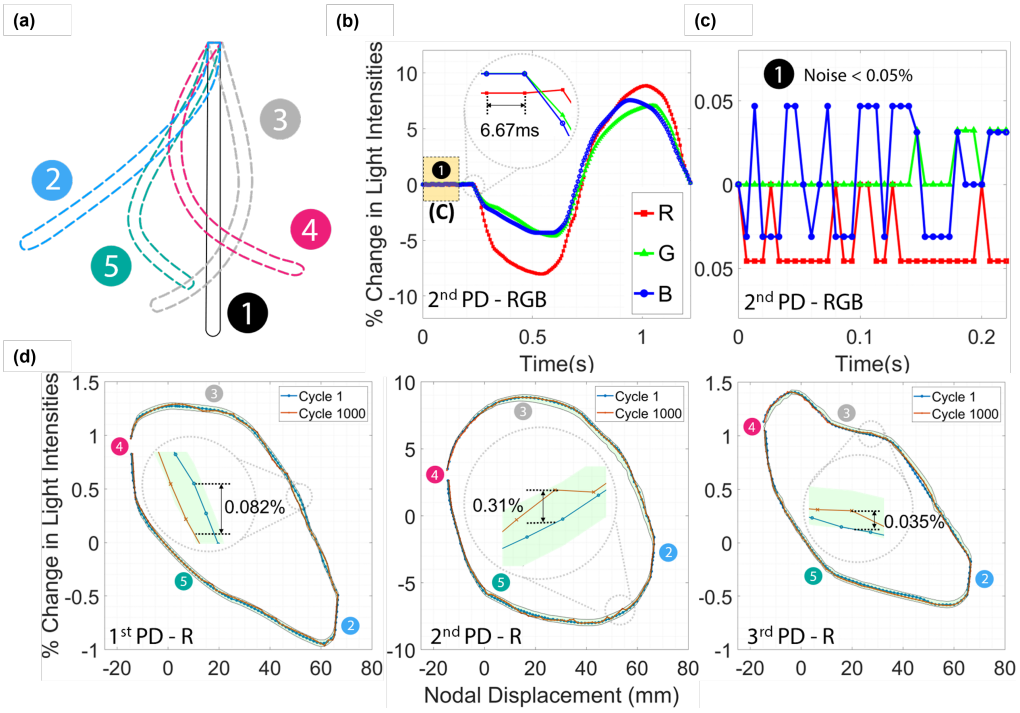

Figure 4.12. Repeatability and hysteresis analysis of the fish-shaped sensor in 1000 cycles of asymmetrical undulating motion underwater. **(a)** Top view of five sensor morphologies. The sensor was deformed in a cyclic mode in sequence ② ③ ④ ⑤, and ① is the initial state) **(b)** RGB light intensity variations of the second pair of LED/PD in the first cycle of motion captured in 150hz. **(c)** Closed-up view of **(b)** at the initial undeformed state (0 to 0.2s). The noise of raw signal is smaller than 0.05%. **(d)** Hysteresis plot of the red light intensity captured by three PDs along with the nodal displacement respectively, where the green shaded region refers to the 95% confidence interval.

with one end clamped (top view initial state ① shown in Figure 4.12**(a)**). The undulating motion was constrained in the cycle, which contained two times of bending leftwards and rightwards (i.e., ② ③ ④ ⑤ in Figure 4.12**(a)**). Initially, the fish-shaped waveguide sensor was kept in the neutral position until 0.2 s as shown in Figure 4.12**(b)**, and three channels of light intensity remained steady with fluctuation less than 0.05% in Figure 4.12**(c)**. The red-light intensities received by three PDs in the 1st and 1,000th cycles were analyzed as displayed in Figure 4.12**(d)**. In terms of a specified nodal displacement, the light intensity changes in these two cycles are nearly the same, the maximum difference of which is less than 0.31%. In conclusion, the results imply that the sensing data

is stable with small noise, and reliable even after 1,000 repeated motion cycles. It also reveals that finite rigidity from tiny LEDs and PDs is not hindering the flexibility of soft sensors, especially in the case of high-order morphology changes involving bending, twisting and stretching. Data communication in an underwater environment (with negligible water pressure) is also stable due to the excellent water-repellent property of silicone PDMS.

4.4 Conclusion

In this Chapter, a shape decoding framework for the light transmission-based soft skin sensor utilizing FEA and deep learning is presented. The FE method plays an important role in the pre-fabrication design analysis of sensor, allowing the optimization of distributing sensing units on the skin sensor with finite computational cost. The effect of distance and angle between LEDs and PDs on light transmission is explored via the FE simulation, and discovered problems of low resolution. Many-to-one in sensing data could have been eliminated after design optimization. The resulting real-time shape decoding performance was demonstrated with simple corner bending. The A5-sized prototype indicates that a relatively short distance (≈75 mm) and large angle (≈90°) between PD and LED could reduce light energy loss and promote data recognizability for data-driven modeling. Interpolation of sparse data using FE simulation provides much more datasets for model training, easing the requirement for the dense distribution of markers on skin sensors for the record of high-resolution and complicated deformation. The skin sensor deformation is described using 48 nodes coordinates interpolated through FEA from five real markers, and thus the dataset including continuous light signal and skin sensor shape was collected. The repeatability test shows that data of the fish shape sensor is reliable even after 1,000-cycle deformation (difference of light intensity < 0.31%) with acceptable noises (< 0.05%). Before training, the

data considering the skin motion was of spatial locality and temporal continuity. Results indicate that grouped node coordinate is in relation to the skin deformation, and ACF reveals both the light signal and node coordinate are affected by their history, respectively. The mapping from light intensity to skin shape based on an autoregressive model is constructed, in which time-window and patch-processing were utilized. The trained model could reconstruct the nodal displacement with RMSE of 0.27 mm (for the 700-frame test data), and the predicted skin shape was close to ground truth even for the complex motion (e.g., a combination of bending and torsion). The ablation study on model architecture implies the three key components of the framework, namely the time window, autoregression and patch-wise processing are beneficial to prediction in view of error.

The proposed LED-PD-based optical sensing could be combined in artificial skin to percept human body motions, or enclosed in soft robots to offer proprioceptive shape information in human-robot interaction. Nevertheless, the study of other sensing modalities have been excluded and the framework was only verified on 3-D morphological changes. Accurate proprioception involving localized pressure (e.g. multi-point fingertips) or stretching needs further research effort. In summary, a shape-sensing framework for an LED-PD-based soft waveguide sensor is developed. The FEA for sparse-to-dense data processing and design optimization, and the autoregressive shape prediction model can also be utilized for other transducing techniques such as electrical-impedance- [111] or acoustic-based methods [106], [112].

Chapter 5

Conclusion

This thesis addresses the research gap in reconstructing high-dimensional shape changes by investigating computational mechanics and data-driven modeling. A real-time shape-sensing framework with a step-by-step workflow was developed and experimentally validated. Multiple sensors with different configurations were prototyped and characterized in terms of repeatability and accuracy. The major achievements are summarized as follows:

5.1 Achievement Summary

1. Thin A4-sized ($210 \times 297 \times 1$ mm) shape sensor that routed FBGs optical fiber on the top surface of silicone rubber, where sensor configuration was optimized through FEA.
2. Optical waveguide sensors with simple optoelectronics, namely LEDs and PDs, to form a self-contained "skin" capable of untethered sensing of shape changes at high frequency (150 Hz)
3. Data-driven modeling approach that makes use of enriched data from FEA, reducing the density of sensor array/transducing units and the complexity of multiplexing/processing its raw signals.

4. An autoregression (AR)-based learning framework for accurately decoding RGB light signals into deformation patterns, which can be a general approach for spatial and temporal sensing data across different sensing modalities.

5. Underwater experimental validation for the proposed shape sensing framework with characterized accuracy and repeatability.

5.2 Future Work

Based on this thesis and the surging trend of artificial intelligence, many possibilities for enhancing the performance and reliability of soft sensing have been opened up. The advantage of deep learning, or the technique of processing vast information, has been substantially validated in building a high-fidelity model in this thesis and many upfront soft sensors. More research can be shifted to investigating a specialized data-driven model for a targeted application and scenario. For instance, tracking human back muscle motion enhances swimming performance. A self-contained artificial skin wearable developed with reference to the presented framework in Chapter 4 may endow the athlete with quantitative kinaesthetic feedback, or the so-called "muscle memory". Alternatively, the sensor can be integrated into a biomimetic soft robot, where the shape-sensing ability acknowledges the deformed robot state in real time. It offers a stereoscopic spatial estimation and shape representation than the sense of touch, and enables further closed-loop control and actuation. Both tasks make use of an object-based experimental dataset, therefore, require iterative computational customization analysis. One possible research direction is to develop a pre-trained transfer model without prior knowledge of targeted systems. The pilot simulated study in Chapter 4 showcases that the spatiotemporal data characteristic is true in waveguide sensing regardless of geometry. The variance in a task may only lead to the

variance in data shape, which eventually could be mapped to repeatable outputs. The changes in training data may stimulate more in-depth investigation into the modeling approach. Sensing feedbacks are mostly local-specific, time-series data, thus usually decoded in the time domain. A state-of-the-art transformer and attention mechanism could be exciting despite conventional classification and regression techniques. The vanilla transformer decoder is autoregressive at inference time, implying that the deformed state of the previous timestamp can be used for the current instance, accompanied by the light signals. This shed insights into constructing a network architecture with spatial and temporal attention blocks, as well as a pre-trained model/encoder used for various applications.

Despite the opportunities in deep learning modeling, the potential of employing computational mechanics in other sensing modalities is also uncovered. Light pressure pressing, stretching of larger %elongation and twisting >360° that have been achieved in some advanced flexible electronics can be explored using the proposed waveguide sensing framework. For instance, using a highly stretchable hydrogel as the waveguide medium with prior knowledge of its material properties. The simulated environment can then be developed with infinite output strains in an infinite possible stretched sensor state. The subsequent training uses noise-free strains at multiple locations and synchronous intensity changes, following the workflow as presented. Besides the waveguide medium, the hardware components and sensor configuration may also be upgraded to optimize light signal quality.

Furthermore, the combined use of computational mechanics and a data-driven learning model could be implemented in other soft sensors, especially those reviewed in Chapter 2. Using consistent simulated data, the density of distributed sensor array could be reduced, as well as the complexity of the electrical connection. For instance, the pressure/strain captured by a

single transducer would be replaced by stresses exerted on the soft substrate over a larger area. Discrete point-wise sensing would become continuous along the entire soft sensor. The groundbreaking sensitivity exhibited by the novel transducing method would also be utilized as constraints/ground truths to confirm the simulated outputs are consistent. To conclude, the framework could minimize transducing units from dense to sparse while providing sensing signals from sparse to dense.

Bibliography

[1] G. Cheng, E. Dean-Leon, F. Bergner, J. R. G. Olvera, Q. Leboutet, and P. Mittendorfer, "A comprehensive realization of robot skin: Sensors, sensing, control, and applications," *Proceedings of the IEEE*, vol. 107, pp. 2034–2051, 10 Oct. 2019, ISSN: 15582256. DOI: 10.1109/JPROC.2019.2933348.

[2] Y. Shao, H. Hu, and Y. Visell, "A wearable tactile sensor array for large area remote vibration sensing in the hand," *IEEE Sensors Journal*, vol. 20, pp. 6612–6623, 12 Jun. 2020, ISSN: 15581748. DOI: 10.1109/JSEN.2020.2972521.

[3] W. W. Lee, Y. J. Tan, H. Yao, *et al.*, "A neuro-inspired artificial peripheral nervous system for scalable electronic skins," *Science Robotics*, vol. 2198, July 2019. DOI: 10.1126/scirobotics.aax2198.

[4] P. Mittendorfer and G. Cheng, "Integrating discrete force cells into multi-modal artificial skin," in *2012 12th IEEE-RAS International Conference on Humanoid Robots (Humanoids 2012)*, IEEE, 2012, pp. 847–852. DOI: 10.1109/HUMANOIDS.2012.6651619.

[5] Y. S. Oh, J.-H. Kim, Z. Xie, *et al.*, "Battery-free, wireless soft sensors for continuous multi-site measurements of pressure and temperature from patients at risk for pressure injuries," *Nature communications*, vol. 12, no. 1, p. 5008, 2021. DOI: 10.1038/s41467-021-25324-w.

[6] Y. Kim, A. Chortos, W. Xu, *et al.*, "A bioinspired flexible organic artificial afferent nerve," *Science*, vol. 360, no. 6392, pp. 998–1003, 2018. DOI: 10.1126/science.aao0098.

[7] W. Gao, H. Ota, D. Kiriya, K. Takei, and A. Javey, "Flexible electronics toward wearable sensing," *Accounts of chemical research*, vol. 52, no. 3, pp. 523–533, 2019. DOI: 10.1021/acs.accounts.8b00500.

[8] K. Bae, J. Jeong, J. Choi, S. Pyo, and J. Kim, "Large-area, crosstalk-free, flexible tactile sensor matrix pixelated by mesh layers," *ACS Applied Materials and Interfaces*, vol. 13, pp. 12 259–12 267, 10 Mar. 2021, ISSN: 19448252. DOI: 10.1021/acsami.0c21671.

[9] S. Lee, S. Franklin, F. A. Hassani, *et al.*, "Nanomesh pressure sensor for monitoring finger manipulation without sensory interference," *Science*, vol. 370, pp. 966–970, 6519 2020. DOI: 10.1126/science.abc9735.

[10] H.-R. Lim, H. S. Kim, R. Qazi, Y.-T. Kwon, J.-W. Jeong, and W.-H. Yeo, "Advanced soft materials, sensor integrations, and applications of wearable flexible hybrid electronics in healthcare, energy, and environment," *Advanced Materials*, vol. 32, no. 15, p. 1 901 924, 2020. DOI: 10.1002/adma.201901924.

[11] Y. Wu, Y. Liu, Y. Zhou, *et al.*, "A skin-inspired tactile sensor for smart prosthetics," *Science Robotics*, vol. 3, no. 22, eaat0429, 2018. DOI: 10.1126/scirobotics.aat0429.

[12] P. Yu, X. Li, H. Li, *et al.*, "All-fabric ultrathin capacitive sensor with high pressure sensitivity and broad detection range for electronic skin," *ACS Applied Materials and Interfaces*, vol. 13, pp. 24 062–24 069, 20 May 2021, ISSN: 19448252. DOI: 10.1021/acsami.1c05478.

[13] W. Lin, B. Wang, G. Peng, *et al.*, "Skin-inspired piezoelectric tactile sensor array with crosstalk-free row+column electrodes for spatiotemporally distinguishing diverse stimuli," *Advanced Science*, vol. 8, p. 2 002 817, 3 Feb. 2021, ISSN: 2198-3844. DOI: 10.1002/ADVS.202002817.

[14] H. Liu, H. Zhao, S. Li, *et al.*, "Adhesion-free thin-film-like curvature sensors integrated on flexible and wearable electronics for monitoring bending of joints and various body gestures," 2018. DOI: 10.1002/admt.201800327.

[15] J. Avery, M. Runciman, C. Fiani, *et al.*, "Lumen shape reconstruction using a soft robotic balloon catheter and electrical impedance tomography," in *2022 IEEE/RSJ International Conference on Intelligent Robots and Systems (IROS)*, IEEE, 2022, pp. 3414–3421. DOI: 10.1109/IROS47612.2022.9981150.

[16] J. Avery, M. Runciman, A. Darzi, and G. P. Mylonas, "Shape sensing of variable stiffness soft robots using electrical impedance tomography," in *2019*

International Conference on Robotics and Automation (ICRA), IEEE, 2019, pp. 9066–9072.

[17] W. Xin, F. Zhu, P. Wang, Z. Xie, Z. Tang, and C. Laschi, "Electrical impedance tomographic shape sensing for soft robots," *IEEE Robotics and Automation Letters*, vol. 8, no. 3, pp. 1555–1562, 2023. DOI: 10.1109/ICRA.2019.8793862.

[18] P. Won, S. Jeong, C. Majidi, and S. H. Ko, "Recent advances in liquid-metal-based wearable electronics and materials," *iScience*, vol. 24, p. 102 698, 7 Jul. 2021, ISSN: 2589-0042. DOI: 10.1016/J.ISCI.2021.102698.

[19] Z. Zhao, S. Soni, T. Lee, *et al.*, "Smart eutectic gallium–indium: From properties to applications," *Advanced Materials*, vol. 35, p. 2 203 391, 1 Jan. 2023, ISSN: 1521-4095. DOI: 10.1002/ADMA.202203391.

[20] Y.-L. Park, B.-R. Chen, and R. J. Wood, "Design and fabrication of soft artificial skin using embedded microchannels and liquid conductors," *IEEE Sensors journal*, vol. 12, no. 8, pp. 2711–2718, 2012. DOI: 10.1109/JSEN.2012.2200790.

[21] Y. Gao, H. Ota, E. W. Schaler, *et al.*, "Wearable microfluidic diaphragm pressure sensor for health and tactile touch monitoring," *Advanced Materials*, vol. 29, p. 1 701 985, 39 Oct. 2017, ISSN: 1521-4095. DOI: 10.1002/ADMA.201701985.

[22] Z. Ma, Q. Huang, Q. Xu, *et al.*, "Permeable superelastic liquid-metal fibre mat enables biocompatible and monolithic stretchable electronics," *Nature Materials 2021 20:6*, vol. 20, pp. 859–868, 6 Feb. 2021, ISSN: 1476-4660. DOI: 10.1038/S41563-020-00902-3.

[23] L. Tang, J. Shang, and X. Jiang, "Multilayered electronic transfer tattoo that can enable the crease amplification effect," *Science Advances*, vol. 7, pp. 3778–3791, 3 Jan. 2021, ISSN: 23752548. DOI: 10.1126/sciadv.abe3778.

[24] J. Tapia, E. Knoop, M. Mutný, M. A. Otaduy, and M. Bächer, "Makesense: Automated sensor design for proprioceptive soft robots," *https://home.liebertpub.com/soro*, vol. 7, pp. 332–345, 3 Jun. 2020, ISSN: 21695180. DOI: 10.1089/SORO.2018.0162.

[25] S. Liu, D. S. Shah, and R. Kramer-Bottiglio, "Highly stretchable multilayer electronic circuits using biphasic gallium-indium," *Nature Materials 2021 20:6*, vol. 20, pp. 851–858, 6 Feb. 2021, ISSN: 1476-4660. DOI: 10.1038/S41563-021-00921-8.

[26] J. Lai, H. Zhou, Z. Jin, *et al.*, "Highly stretchable, fatigue-resistant, electrically conductive, and temperature-tolerant ionogels for high-performance flexible sensors," *ACS Applied Materials and Interfaces*, vol. 11, pp. 26 412–26 420, 29 Jul. 2019, ISSN: 19448252. DOI: 10.1021/acsami.9b10146.

[27] Y. Liang, L. Ye, X. Sun, Q. Lv, and H. Liang, "Tough and stretchable dual ionically cross-linked hydrogel with high conductivity and fast recovery property for high-performance flexible sensors," *ACS Applied Materials and Interfaces*, vol. 12, pp. 1577–1587, 1 Jan. 2020, ISSN: 19448252. DOI: 10.1021/acsami.9b18796.

[28] S. Huang, Y. Liu, Y. Zhao, Z. Ren, and C. F. Guo, "Flexible electronics: Stretchable electrodes and their future," *Advanced Functional Materials*, vol. 29, no. 6, p. 1 805 924, 2019. DOI: 10.1002/adfm.201805924.

[29] J. Tao, H. Khosravi, V. Deshpande, and S. Li, "Engineering by cuts: How kirigami principle enables unique mechanical properties and functionalities," 2022. DOI: 10.1002/advs.202204733.

[30] S. Jiang, J. Liu, W. Xiong, *et al.*, "A snakeskin-inspired, soft-hinge kirigami metamaterial for self-adaptive conformal electronic armor," *Advanced Materials*, vol. 34, no. 31, p. 2 204 091, 2022. DOI: 10.1002/adma.202204091.

[31] Y. G. Kim, J. H. Song, S. Hong, and S. H. Ahn, "Piezoelectric strain sensor with high sensitivity and high stretchability based on kirigami design cutting," *npj Flexible Electronics 2022 6:1*, vol. 6, pp. 1–8, 1 Jun. 2022, ISSN: 2397-4621. DOI: 10.1038/s41528-022-00186-4.

[32] C. M. Boutry, M. Negre, M. Jorda, *et al.*, "A hierarchically patterned, bioinspired e-skin able to detect the direction of applied pressure for robotics," *Science Robotics*, vol. 3, 24 Nov. 2018, ISSN: 24709476. DOI: 10.1126/scirobotics.aau6914.

[33] A. Rafsanjani and K. Bertoldi, "Buckling-induced kirigami," 2017. DOI: 10.1103/PhysRevLett.118.084301.

[34] H. Liu, H. Li, Z. Wang, *et al.*, "Robust and multifunctional kirigami electronics with a tough and permeable aramid nanofiber framework," *Advanced Materials*, p. 2 207 350, 2022. DOI: 10.1002/adma.202207350.

[35] E. E. Evke, D. Meli, M. Shtein, E. E. Evke, D. Meli, and M. Shtein, "Developable rotationally symmetric kirigami-based structures as sensor platforms," *Advanced Materials Technologies*, vol. 4, p. 1 900 563, 12 Dec. 2019, ISSN: 2365-709X. DOI: 10.1002/ADMT.201900563.

[36] A. Hermanis, R. Cacurs, and M. Greitans, "Acceleration and magnetic sensor network for shape sensing," *IEEE Sensors Journal*, vol. 16, pp. 1271–1280, 5 Mar. 2016, ISSN: 1530437X. DOI: 10.1109/JSEN.2015.2496283.

[37] S. Dong, W. Yuan, and E. H. Adelson, "Improved gelsight tactile sensor for measuring geometry and slip," in *2017 IEEE/RSJ International Conference on Intelligent Robots and Systems (IROS)*, IEEE, 2017, pp. 137–144. DOI: 10.1109/IROS.2017.8202149.

[38] Y. Han, A. Varadarajan, T. Kim, *et al.*, "Smart skin: Vision-based soft pressure sensing system for in-home hand rehabilitation," *Soft Robotics*, vol. 9, no. 3, pp. 473–485, 2022. DOI: 10.1089/soro.2020.0083.

[39] H. Sun, K. J. Kuchenbecker, and G. Martius, "A soft thumb-sized vision-based sensor with accurate all-round force perception," *Nature Machine Intelligence*, vol. 4, no. 2, pp. 135–145, 2022. DOI: 10.1038/s42256-021-00439-3.

[40] B. Ward-Cherrier, N. Pestell, L. Cramphorn, *et al.*, "The tactip family: Soft optical tactile sensors with 3d-printed biomimetic morphologies," *Soft robotics*, vol. 5, no. 2, pp. 216–227, 2018. DOI: 10.1089/soro.2017.0052.

[41] C. Chorley, C. Melhuish, T. Pipe, and J. Rossiter, "Development of a tactile sensor based on biologically inspired edge encoding," in *2009 International Conference on Advanced Robotics*, IEEE, 2009, pp. 1–6.

[42] P. Lu, N. Lalam, M. Badar, *et al.*, "Distributed optical fiber sensing: Review and perspective," *Applied Physics Reviews*, vol. 6, no. 4, p. 041 302, 2019.

[43] I. Floris, J. M. Adam, P. A. Calderón, and S. Sales, *Fiber optic shape sensors: A comprehensive review*, Apr. 2021. DOI: 10.1016/j.optlaseng.2020.106508.

[44] P. Li, C. Fu, B. Du, *et al.*, "High-spatial-resolution strain sensor based on distance compensation and image wavelet denoising method in ofdr," *Journal of Lightwave Technology*, vol. 39, no. 19, pp. 6334–6339, 2021. DOI: 10.1109/JLT.2021.3095851.

[45] M. Luo, J. Liu, C. Tang, X. Wang, T. Lan, and B. Kan, "0.5 mm spatial resolution distributed fiber temperature and strain sensor with position-deviation compensation based on ofdr," *Optics express*, vol. 27, no. 24, pp. 35 823–35 829, 2019. DOI: 10.1364/OE.27.035823.

[46] Y. Noh, H. Liu, S. Sareh, *et al.*, "Image-based optical miniaturized three-axis force sensor for cardiac catheterization," *IEEE Sensors Journal*, vol. 16, pp. 7924–7932, 22 Nov. 2016, ISSN: 1530437X. DOI: 10.1109/JSEN.2016.2600671.

[47] F. Khan, A. Denasi, D. Barrera, J. Madrigal, S. Sales, and S. Misra, "Multi-core optical fibers with bragg gratings as shape sensor for flexible medical instruments; multi-core optical fibers with bragg gratings as shape sensor for flexible medical instruments," *IEEE Sensors Journal*, vol. 19, 14 2019. DOI: 10.1109/JSEN.2019.2905010.

[48] D. Paloschi, K. A. Bronnikov, S. Korganbayev, A. A. Wolf, A. Dostovalov, and P. Saccomandi, "3d shape sensing with multicore optical fibers: Transformation matrices versus frenet-serret equations for real-time application," *IEEE Sensors Journal*, vol. 21, no. 4, pp. 4599–4609, 2020. DOI: 10.1109/JSEN.2020.3032480.

[49] Z. Dong, X. Wang, G. Fang, *et al.*, "Shape tracking and feedback control of cardiac catheter using mri-guided robotic platform—validation with pulmonary vein isolation simulator in mri," *IEEE Transactions on Robotics*, vol. 38, no. 5, pp. 2781–2798, 2022. DOI: 10.1109/TRO.2022.3154691.

[50] T. L. T. Lun, K. Wang, J. D. Ho, K.-H. Lee, K. Y. Sze, and K.-W. Kwok, "Real-time surface shape sensing for soft and flexible structures using fiber bragg gratings," *IEEE Robotics and Automation Letters*, vol. 4, no. 2, pp. 1454–1461, 2019. DOI: 10.1109/LRA.2019.2893036.

[51] T. Li, Y. Su, F. Chen, *et al.*, "A skin-like and highly stretchable optical fiber sensor with the hybrid coding of wavelength–light intensity," *Advanced Intelligent Systems*, vol. 4, no. 4, p. 2 100 193, 2022. DOI: 10.1002/aisy.202100193.

[52] Q. Hou, C. Lu, X. Li, and T. Han, "Sensing model fbg-based used for position and orientation detection of soft manipulator," *IEEE Sensors Journal*, vol. 21, no. 21, pp. 24 218–24 225, 2021. DOI: 10.1109/JSEN.2021.3110987.

[53] K. Wang, C.-H. Mak, J. D. L. Ho, *et al.*, "Large-scale surface shape sensing with learning-based computational mechanics," *Advanced Intelligent Systems*, vol. 3, p. 2 100 089, 11 Nov. 2021, ISSN: 2640-4567. DOI: 10.1002/AISY.202100089.

[54] H. Bezawada, C. Woods, and V. Vikas, "Shape reconstruction of soft manipulators using vision and imu feedback," *IEEE Robotics and Automation Letters*, vol. 7, pp. 9589–9596, 4 Oct. 2022, ISSN: 23773766. DOI: 10.1109/LRA.2022.3191523.

[55] T. Li, L. Qiu, H. Ren,) L. Qiu, and H. Ren, "Distributed curvature sensing and shape reconstruction for soft manipulators with irregular cross sections based on parallel dual-fbg arrays," *TRANSACTIONS ON MECHATRONICS*, vol. 25, 1 2020. DOI: 10.1109/TMECH.2019.2949151.

[56] K. C. Galloway, Y. Chen, E. Templeton, B. Rife, I. S. Godage, and E. J. Barth, "Fiber optic shape sensing for soft robotics," *Soft Robotics*, vol. 6, pp. 671–684, 5 Oct. 2019, ISSN: 21695180. DOI: 10.1089/soro.2018.0131.

[57] X. Wang, G. Fang, K. Wang, *et al.*, "Eye-in-hand visual servoing enhanced with sparse strain measurement for soft continuum robots," *IEEE Robotics and Automation Letters*, vol. 5, pp. 2161–2168, 2 Apr. 2020, ISSN: 23773766. DOI: 10.1109/LRA.2020.2969953.

[58] K. W. Kwok, H. Wurdemann, A. Arezzo, A. Menciassi, and K. Althoefer, "Soft robot-assisted minimally invasive surgery and interventions: Advances and outlook," *Proceedings of the IEEE*, vol. 110, pp. 871–892, 7 Jul. 2022, ISSN: 15582256. DOI: 10.1109/JPROC.2022.3167931.

[59] M. Amanzadeh, S. M. Aminossadati, M. S. Kizil, and A. D. Rakić, "Recent developments in fibre optic shape sensing," *Measurement: Journal of the International Measurement Confederation*, vol. 128, pp. 119–137, Nov. 2018, ISSN: 02632241. DOI: 10.1016/j.measurement.2018.06.034.

[60] J. Guo, K. Zhao, B. Zhou, *et al.*, "Wearable and skin-mountable fiber-optic strain sensors interrogated by a free-running, dual-comb fiber laser," *Advanced Optical Materials*, vol. 7, p. 1 900 086, 12 Jun. 2019, ISSN: 2195-1071. DOI: 10.1002/ADOM.201900086.

[61] C. B. Teeple, K. P. Becker, and R. J. Wood, "Soft curvature and contact force sensors for deep-sea grasping via soft optical waveguides," in *2018 IEEE/RSJ*

International Conference on Intelligent Robots and Systems (IROS), IEEE, 2018, pp. 1621–1627. DOI: 10.1109/IROS.2018.8594270.

[62] H. Zhao, K. O'Brien, S. Li, and R. F. Shepherd, "Optoelectronically innervated soft prosthetic hand via stretchable optical waveguides," *Science Robotics*, vol. 1, 1 Dec. 2016, ISSN: 24709476. DOI: 10.1126/scirobotics.aai7529.

[63] H. Bai, S. Li, J. Barreiros, Y. Tu, C. R. Pollock, and R. F. Shepherd, "Stretchable distributed fiber-optic sensors," *Science*, vol. 852, pp. 848–852, November 2020. DOI: 10.1126/science.aba5504.

[64] C. To, T. L. Hellebrekers, and Y. L. Park, "Highly stretchable optical sensors for pressure, strain, and curvature measurement," *IEEE International Conference on Intelligent Robots and Systems*, vol. 2015-Decem, pp. 5898–5903, 2015, ISSN: 21530866. DOI: 10.1109/IROS.2015.7354215.

[65] W. Chen, C. Xiong, C. Liu, P. Li, and Y. Chen, "Fabrication and dynamic modeling of bidirectional bending soft actuator integrated with optical waveguide curvature sensor," *Soft Robotics*, vol. 6, pp. 495–506, 4 Aug. 2019, ISSN: 21695180. DOI: 10.1089/soro.2018.0061.

[66] H. Bai, Y. S. Kim, and R. F. Shepherd, "Autonomous self-healing optical sensors for damage intelligent soft-bodied systems," *Science Advances*, vol. 8, no. 49, eabq2104, 2022. DOI: 10.1126/sciadv.abq2104.

[67] C. Rendl, D. Kim, S. Fanello, *et al.*, "Flexsense: A transparent self-sensing deformable surface," in *Proceedings of the 27th annual ACM symposium on User interface software and technology*, 2014, pp. 129–138. DOI: 10.1145/2642918.2647405.

[68] I. Van Meerbeek, C. De Sa, and R. Shepherd, "Soft optoelectronic sensory foams with proprioception," *Science Robotics*, vol. 3, no. 24, eaau2489, 2018. DOI: 10.1126/scirobotics.aau2489.

[69] D. Coric, M. Lai, J. Botsis, A. Luo, and H. G. Limberger, "Distributed strain measurements using fiber bragg gratings in small-diameter optical fiber and low-coherence reflectometry," *Optics express*, vol. 18, no. 25, pp. 26 484–26 491, 2010. DOI: 10.1364/OE.18.026484.

[70] Y. Han, A. D. Rogalsky, B. Zhao, and H. J. Kwon, "The application of digital image techniques to determine the large stress–strain behaviors of soft

materials," *Polymer Engineering & Science*, vol. 52, no. 4, pp. 826–834, 2012. DOI: 10.1002/pen.22149.

[71] R. H. Pritchard, P. Lava, D. Debruyne, and E. M. Terentjev, "Precise determination of the poisson ratio in soft materials with 2d digital image correlation," *Soft Matter*, vol. 9, no. 26, pp. 6037–6045, 2013. DOI: 10.1039/C3SM50901J.

[72] A. J. Sadowski and J. M. Rotter, "Solid or shell finite elements to model thick cylindrical tubes and shells under global bending," *International Journal of Mechanical Sciences*, vol. 74, pp. 143–153, 2013. DOI: 10.1016/j.ijmecsci.2013.05.008.

[73] M. Kreuzer, "Strain measurement with fiber bragg grating sensors," *HBM, Darmstadt, S2338-1.0 e*, vol. 12, 2006.

[74] O. Bauchau and J. Craig, "Kirchhoff plate theory," *Structural analysis*, pp. 819–914, 2009. DOI: 10.1007/978-90-481-2516-6_16.

[75] J. Ge, A. E. James, L. Xu, Y. Chen, K.-W. Kwok, and M. P. Fok, "Bidirectional soft silicone curvature sensor based on off-centered embedded fiber bragg grating," *IEEE photonics technology letters*, vol. 28, no. 20, pp. 2237–2240, 2016. DOI: 10.1109/LPT.2016.2590984.

[76] K.-H. Lee, D. K. Fu, M. C. Leong, *et al.*, "Nonparametric online learning control for soft continuum robot: An enabling technique for effective endoscopic navigation," *Soft robotics*, vol. 4, no. 4, pp. 324–337, 2017. DOI: 10.1089/soro.2016.0065.

[77] A. Mendizabal, P. Márquez-Neila, and S. Cotin, "Simulation of hyperelastic materials in real-time using deep learning," *Medical image analysis*, vol. 59, p. 101 569, 2020. DOI: 10.1016/j.media.2019.101569.

[78] F. Roewer-Despres, N. Khan, and I. Stavness, "Towards finite element simulation using deep learning," in *15th international symposium on computer methods in biomechanics and biomedical engineering*, 2018, p. 2018.

[79] R. Phellan, B. Hachem, J. Clin, J. M. Mac-Thiong, and L. Duong, "Real-time biomechanics using the finite element method and machine learning: Review and perspective," *Medical physics*, vol. 48, pp. 7–18, 1 Jan. 2021, ISSN: 2473-4209. DOI: 10.1002/MP.14602.

[80] S. Cuomo, A. Galletti, G. Giunta, and L. Marcellino, "A novel triangle-based method for scattered data interpolation," *Applied Mathematical Sciences*, vol. 8, no. 134, pp. 6717–6724, 2014. DOI: 10.12988/ams.2014.49686.

[81] R. Polikar, "Ensemble learning," *Ensemble machine learning: Methods and applications*, pp. 1–34, 2012. DOI: 10.1007/978-1-4419-9326-7_1.

[82] X. Dong, Z. Yu, W. Cao, Y. Shi, and Q. Ma, "A survey on ensemble learning," *Frontiers of Computer Science*, vol. 14, pp. 241–258, 2020. DOI: 10.1007/s11704-019-8208-z.

[83] A. Helwan and D. Uzun Ozsahin, "Sliding window based machine learning system for the left ventricle localization in mr cardiac images," *Applied Computational Intelligence and Soft Computing*, vol. 2017, pp. 1–9, 2017. DOI: 10.1155/2017/3048181.

[84] R. Lian and L. Huang, "Deepwindow: Sliding window based on deep learning for road extraction from remote sensing images," *IEEE Journal of Selected Topics in Applied Earth Observations and Remote Sensing*, vol. 13, pp. 1905–1916, 2020. DOI: 10.1109/JSTARS.2020.2983788.

[85] O. Sagi and L. Rokach, "Ensemble learning: A survey," *Wiley Interdisciplinary Reviews: Data Mining and Knowledge Discovery*, vol. 8, no. 4, e1249, 2018. DOI: 10.1002/widm.1249.

[86] L. Breiman, "Bagging predictors," *Machine learning*, vol. 24, pp. 123–140, 1996. DOI: 10.1007/BF00058655.

[87] F. Liu, S. Deswal, A. Christou, Y. Sandamirskaya, M. Kaboli, and R. Dahiya, "Neuro-inspired electronic skin for robots," *Science Robotics*, vol. 7, 67 Jun. 2022, ISSN: 24709476. DOI: 10.1126/scirobotics.abl7344.

[88] A. Chortos, J. Liu, and Z. Bao, "Pursuing prosthetic electronic skin," *Nature Materials 2016 15:9*, vol. 15, pp. 937–950, 9 Jul. 2016, ISSN: 1476-4660. DOI: 10.1038/NMAT4671.

[89] G. Pang, G. Yang, and Z. Pang, "Review of robot skin: A potential enabler for safe collaboration, immersive teleoperation, and affective interaction of future collaborative robots," *IEEE Transactions on Medical Robotics and Bionics*, vol. 3, pp. 681–700, 3 Aug. 2021. DOI: 10.1109/TMRB.2021.3097252.

[90] G. Li, X. Chen, F. Zhou, *et al.*, "Self-powered soft robot in the mariana trench," *Nature*, vol. 591, no. 7848, pp. 66–71, 2021. DOI: 10.1038/s41586-020-03153-z.

[91] S. Aracri, F. Giorgio-Serchi, G. Suaria, *et al.*, "Soft robots for ocean exploration and offshore operations: A perspective," *Soft Robotics*, vol. 8, no. 6, pp. 625–639, 2021. DOI: 10.1089/soro.2020.0011.

[92] A. Ramezani, S.-J. Chung, and S. Hutchinson, "A biomimetic robotic platform to study flight specializations of bats," *Science Robotics*, vol. 2, no. 3, eaal2505, 2017. DOI: 10.1126/scirobotics.aal2505.

[93] C. Wu, X. Liu, and Y. Ying, "Soft and stretchable optical waveguide: Light delivery and manipulation at complex biointerfaces creating unique windows for on-body sensing," *ACS Sensors*, vol. 6, pp. 1446–1460, 4 Apr. 2021, ISSN: 23793694. DOI: 10.1021/acssensors.0c02566.

[94] A. W. Snyder and J. Love, *Optical waveguide theory*. Springer Science & Business Media, 2012, ISBN: 1461328136.

[95] H. Krauss and K. Takemura, "Stretchable optical waveguide sensor capable of two-degree-of-freedom strain sensing mediated by a semidivided optical core," *IEEE/ASME Transactions on Mechatronics*, vol. 27, pp. 2151–2157, 4 Aug. 2022, ISSN: 1941014X. DOI: 10.1109/TMECH.2022.3175205.

[96] S. Chen, Z. Li, Y. Lin, F. Wang, and Q. Cao, "Automatic ultrasound scanning robotic system with optical waveguide-based force measurement," *International Journal of Computer Assisted Radiology and Surgery 2021 16:6*, vol. 16, pp. 1015–1025, 6 May 2021, ISSN: 1861-6429. DOI: 10.1007/S11548-021-02385-2.

[97] J. Jung, M. Park, D. Kim, and Y. L. Park, "Optically sensorized elastomer air chamber for proprioceptive sensing of soft pneumatic actuators," *IEEE Robotics and Automation Letters*, vol. 5, pp. 2333–2340, 2 2020, ISSN: 23773766. DOI: 10.1109/LRA.2020.2970984.

[98] Y. Yi, J.-H. Youn, K.-U. Kyung, and D.-S. Kwon, "Embeddable coiled soft sensor-based joint angle sensing for flexible surgical manipulator," *2022 IEEE/RSJ International Conference on Intelligent Robots and Systems (IROS)*, pp. 6906–6912, Oct. 2022. DOI: 10.1109/IROS47612.2022.9981505.

[99] H. Xie, A. Jiang, H. A. Wurdemann, H. Liu, L. D. Seneviratne, and K. Althoefer, "Magnetic resonance-compatible tactile force sensor using fiber optics and vision sensor," *IEEE Sensors Journal*, vol. 14, pp. 829–838, 3 Mar. 2014, ISSN: 1530437X. DOI: 10.1109/JSEN.2013.2281591.

[100] P. Polygerinos, L. D. Seneviratne, and K. Althoefer, "Modeling of light intensity-modulated fiber-optic displacement sensors," *IEEE Transactions on Instrumentation and Measurement*, vol. 60, pp. 1408–1415, 4 Apr. 2011, ISSN: 00189456. DOI: 10.1109/TIM.2010.2085270.

[101] S. Li, H. Bai, R. F. Shepherd, and H. Zhao, "Bio-inspired design and additive manufacturing of soft materials, machines, robots, and haptic interfaces," *Angewandte Chemie International Edition*, vol. 58, pp. 11 182–11 204, 33 Aug. 2019, ISSN: 1521-3773. DOI: 10.1002/ANIE.201813402.

[102] K. Chin, T. Hellebrekers, and C. Majidi, "Machine learning for soft robotic sensing and control," *Advanced Intelligent Systems*, vol. 2, p. 1 900 171, 6 2020, ISSN: 2640-4567. DOI: 10.1002/aisy.201900171.

[103] H. Park, K. Park, S. Mo, and J. Kim, "Deep neural network based electrical impedance tomographic sensing methodology for large-area robotic tactile sensing," *IEEE Transactions on Robotics*, vol. 37, pp. 1570–1583, 5 Oct. 2021, ISSN: 19410468. DOI: 10.1109/TRO.2021.3060342.

[104] C. Larson, J. Spjut, R. Knepper, and R. Shepherd, "A deformable interface for human touch recognition using stretchable carbon nanotube dielectric elastomer sensors and deep neural networks," *https://home.liebertpub.com/soro*, vol. 6, pp. 611–620, 5 Oct. 2019, ISSN: 21695180. DOI: 10.1089/SORO.2018.0086.

[105] T. G. Thuruthel, B. Shih, C. Laschi, and M. T. Tolley, "Soft robot perception using embedded soft sensors and recurrent neural networks," *Science Robotics*, vol. 4, 26 Jan. 2019, ISSN: 24709476. DOI: 10.1126/scirobotics.aav1488.

[106] K. Park, H. Yuk, M. Yang, J. Cho, H. Lee, and J. Kim, "A biomimetic elastomeric robot skin using electrical impedance and acoustic tomography for tactile sensing," *Science Robotics*, vol. 7, 67 Jun. 2022, ISSN: 24709476. DOI: 10.1126/scirobotics.abm7187.

[107] F. Schneider, J. Draheim, R. Kamberger, and U. Wallrabe, "Process and material properties of polydimethylsiloxane (pdms) for optical mems," *Sensors and Actuators A*, vol. 151, pp. 95–99, 2009. DOI: 10.1016/j.sna.2009.01.026.

[108] G. E. Box, G. M. Jenkins, G. C. Reinsel, and G. M. Ljung, *Time series analysis: forecasting and control*. John Wiley & Sons, 2015.

[109] A. Müller, M. C. Wapler, and U. Wallrabe, "A quick and accurate method to determine the poisson's ratio and the coefficient of thermal expansion of pdms," *Soft Matter*, vol. 15, pp. 779–784, 4 Jan. 2019, ISSN: 17446848. DOI: 10.1039/C8SM02105H.

[110] R. Moučka, M. Sedlačík, J. Osička, and V. Pata, "Mechanical properties of bulk sylgard 184 and its extension with silicone oil," *Scientific Reports 2021 11:1*, vol. 11, pp. 1–9, 1 Sep. 2021, ISSN: 2045-2322. DOI: 10.1038/s41598-021-98694-2.

[111] H. Chen, X. Yang, J. Geng, G. Ma, and X. Wang, "A convolutional neural network based electrical impedance tomography method for skin-like hydrogel sensing," *2022 IEEE International Conference on Robotics and Biomimetics (ROBIO)*, pp. 178–183, Dec. 2022. DOI: 10.1109/ROBIO55434.2022.10011766.

[112] J. B. Chossat and P. B. Shull, "Soft acoustic waveguides for strain, deformation, localization, and twist measurements," *IEEE Sensors Journal*, vol. 21, pp. 222–230, 1 Jan. 2021, ISSN: 15581748. DOI: 10.1109/JSEN.2020.3013067.